This manuscript has been submitted to the Quarterly Journal of the Royal Meteorological Society and has not been peer-reviewed.

ORIGINAL ARTICLE

Journal Section

Large-scale controls on intensity-duration characteristics of heatwaves in an idealised model

Abel Shibu[1*] | Joy Monteiro[2,3]

[1]Department of Physics, Imperial College London, London SW7 2AZ, United Kingdom

[2]Department of Earth and Climate Science, Indian Institute of Science Education and Research Pune, Pune, India

[3]Department of Data Science, Indian Institute of Science Education and Research Pune, Pune, India

Correspondence
Abel Shibu, Department of Physics, Imperial College London, London SW7 2AZ, United Kingdom.
Email: abels2000@gmail.com

Funding information

The relationship between the large-scale structure of the

[*]Part of this work was conducted when affiliated to IISER Pune

atmospheric circulation and the mean intensity and duration of heatwaves is studied in an idealised climate model. Using the tight relationship between near-surface temperature and lower tropospheric dry static energy (DSE) in the model, we study the energetics of the lower troposphere during heatwaves in the model. This analysis leads to a quantitative framework to partition intensity and duration of heatwaves to different components of advection and identify the main contributors. We observe that while contribution of the meridional advection of DSE explains the difference between high and low intensity heatwaves in a given location, it does not explain variation of mean intensity across latitudes. In a similar manner, we find that while the contribution of meridional advection is important in explaining the difference between high and low duration heatwaves in a given location, it does not explain variation of mean duration across latitudes. We find that the zonal advection of DSE plays an important role in explaining variation of mean intensity and duration of heatwaves across latitudes. By linking these advective terms to the variation of the lower-tropospheric circulation across latitudes, we present an explanation of how the general circulation of the atmosphere – particularly the location of the storm track – controls the mean intensity and duration of heatwaves in our model.

KEYWORDS

heatwaves, atmospheric circulation, idealised modelling, extreme events, heatwave intensity and duration

1 | INTRODUCTION

Heatwaves are periods of extremely high near-surface temperature, and are usually defined as discrete events (or periods of time) when the exceedance of a certain threshold of two-meter temperature is observed (Perkins and Alexander, 2012). This event-based definition of heatwaves naturally leads to the question of characterising such events, and heatwaves are typically described by their intensity-duration-frequency characteristics (Perkins and Alexander, 2012; Perkins, 2015), with intensity and duration being characteristics of individual events whereas frequency is an inter-event characteristic.

The contribution to the lifecycle of a heatwave can be separated into two distinct kinds (See Röthlisberger and Papritz, 2023, for example):

- Adiabatic contribution – The presence of anticyclones which lead to subsidence-driven heating and the transport of heat across climatological gradients of dry static energy by the atmospheric circulation.
- Diabatic or boundary contribution – Increased sensible heat fluxes due to a combination of enhanced shortwave radiation (due to the reduction in cloudiness by the anticyclone-driven subsidence) and/or surface characteristics such as vegetation and soil moisture which could enhance sensible heat fluxes.

The role of the atmospheric circulation – particularly quasi-stationary Rossby wave packets and blocking events have been extensively studied (See Barriopedro et al., 2023, and references therein). However, a large number of (primarily mid-latitude) studies from across the world have suggested that heatwave intensity and duration are primarily controlled by the boundary contribution and feedbacks with the boundary layer, with the large-scale circulation playing a secondary role (see reviews by Perkins, 2015; Domeisen et al., 2022, and references therein). In monsoonal regions like South Asia – where the heatwave season is actually spring and not summer, cloudiness is at a annual minimum during the heatwave (or pre-monsoon) season due to its location below the subsiding branch of the Hadley cell. Therefore, large changes in shortwave forcing during heatwaves is unlikely. Furthermore, soil moisture is climatologically at its minimum value as well during this season. This situation opens up the possibility that the circulation could play a more important role during heatwaves in such regions.

The literature above mostly discusses the impacts of the dynamics and local factors in the context of *individual* heatwaves. In this study, we focus on how the large-scale circulation might determine the *long-term statistics* of heatwaves in a particular location, particularly their mean intensity and duration. A second line of literature looks at how the large-scale circulation controls the probability density function (PDF) of temperature (Schneider et al., 2014; Garfinkel and Harnik, 2016; Linz et al., 2018; Tamarin-Brodsky et al., 2019), but the focus is on the moments (variance and/or skewness) of the entire PDF of temperature rather than characteristics of heatwaves. Furthermore, the focus is usually on free tropospheric rather than near-surface temperatures.

Quantifying the contribution of circulation related controls to heatwave characteristics in observations is challenging due to the strong influence of the boundary in determining near-surface temperatures. One potential way forward is to use idealised models where the boundary effects are less important (Jiménez-Esteve et al., 2022; Jiménez-Esteve and Domeisen, 2022). In this study, we use an idealised climate model which is configured to reduce boundary effects on heatwaves and study the contribution of the circulation to the lower-tropospheric dry static energy (DSE) budget. Since DSE is conserved by the flow, it is possible to quantify the contribution of the individual components of the circulation in an unambiguous manner. By relating DSE to near-surface temperature, we are then able to develop a quantitative framework to partition intensity and duration contributions into the individual components of the circulation. We use this framework to quantify the contributions of individual components of the circulation, and then examine how these components are influenced by the large-scale circulation. This two-stage analysis allows us to link mean intensity and duration characteristics of heatwaves to the large-scale circulation.

2 | METHODS

2.1 | Model description

For this study, we use an idealised general circulation model (GCM) created using the climt modelling toolkit (Monteiro et al., 2018). Our GCM configuration is similar to the model setup in Frierson et al. (2006). To summarise, our model has a slab ocean and a zonally symmetrical land configuration, with the grids between 20° and 60° in both hemispheres set as land grids. The ocean and land grids only differ in their depth, heat capacity and surface relative humidity. The land grids have a prescribed depth value of 1 m and a heat capacity value of 2000 $Jkg^{-1}K^{-1}$. For the ocean, the prescribed depth value is 2 m, with the heat capacity being the heat capacity of water, 4182 $Jkg^{-1}K^{-1}$. This models the higher heat capacity of the ocean relative to land, and the relatively low prescribed depth values minimises the effect of long-memory surface processes.

The relative humidity at the ocean surface is set to the saturation specific humidity at the surface temperature. For the land grids, we set the relative humidity at the land surface to be 70% of the saturation specific humidity. This models the lower moisture availability over land relative to the ocean and modifies the ratio of Sensible Heat Flux (SHF) to Latent Heat Flux (LHF) over land. The temperature of the surface is controlled dynamically by the energy balance at the surface. There is no topography in our model.

The surface flux and boundary layer formulation is as in Frierson et al. (2006). A gray radiation scheme is used, with values for atmosphere opacity τ prescribed as

$$\tau = [\tau_{0e} + (\tau_{0p} - \tau_{0e})\sin^2(\phi)]\left(\frac{p}{p_s}\right) \tag{1}$$

where $\tau_{0p} = 1.5$ and $\tau_{0e} = 6$ are values of atmosphere opacity at the surface at the pole and equator, respectively. p and p_s are pressure and surface pressure respectively and ϕ is the latitude. The vertical profile of optical depth with pressure in our model is linear, unlike in Frierson et al. (2006), where a combination of linear and quartic terms were used. The incoming solar flux values R_s has an off-equatorial maximum, with maximum flux at 10°N, and decreasing towards the poles with functional form

$$R_s(\phi) = \begin{cases} R_{max}[1 + \Delta_s p_2(\phi - 10^\circ)] & \text{for } \phi \geq -80^\circ \\ R_{max}[1 + \Delta_s p_2(-90^\circ)] & \text{otherwise} \end{cases} \tag{2}$$

where $p_2(\theta) = \frac{1}{4}[1 - 3\sin^2\theta]$ is the second Legendre polynomial and ϕ is the latitude. $R_{max} = 150$ Wm^{-2} and $\Delta_s = 1.4$ sets the meridional gradient of solar flux. The model is in perpetual forcing, and has no seasonality or diurnal cycle. Moist convection in the model is parameterized using the Emanuel convection scheme (Emanuel and Živković Rothman, 1999). The model does not include clouds or sea ice.

A spectral dynamical core solves the primitive equations and is run at T42 grid resolution (64 x 128, 2.76° x 2.79°), which equates to a grid length of approximately 310 km at the equator. The model has 28 height levels and an integration time step of 20 minutes. This model was run for a duration of 1000 years and the model variables are saved as a daily average for each day. The spinup time of the model, the time for the model's climate to equilibrate, is around a year. We have spun up the model for 3 years to ensure that equilibrium is reached.

| Model climatology

A 30-year climatology of our model is shown in Fig. 1. As the maximum insolation is at 10°N, the temperature maximum is in the northern hemisphere (Fig. 1, panels a and b). The subtropical jet stream, which marks the meridional extent of the Hadley circulation is stronger in the winter hemisphere. Similarly, the eddy-driven jet – marked by the location of the maxima in meridional wind variance, is also stronger in the winter hemisphere (both from the mean meridional mass streamfunction and the mean meridional wind variance in panels c and d). The zonal wind maximum in the northern hemisphere is at around 54°N, over the poleward flank of the land region, while the corresponding maximum in the southern hemisphere is at around 26°S. The maximum jet speed in the northern hemisphere is around 27 ms^{-1}, and around 51 ms^{-1} the southern hemisphere. In both hemispheres, the location of the baroclinic zones – characterised by enhanced eddy activity and large variance of the meridional winds – is poleward of the subtropical jet itself and marks the latitude of the eddy-driven jet (Lee and Kim, 2003). The momentum flux convergence in these baroclinic zones leads to the development of climatological surface westerlies at the same latitude (panels b and c). Consistent with the counterpropagating Rossby edge wave picture of baroclinic instability (Hoskins et al., 1985; Heifetz et al., 2004), the free-tropospheric meridional wind variance maxima are accompanied by a corresponding lower-tropospheric counterpart (panel d). The global mean sensible and latent heat fluxes over land are about 8.2 Wm^{-2} and 47.9 Wm^{-2}, suggesting that surface exchange over land is dominated by latent heat fluxes in our model configuration.

2.2 | Heatwaves

Since we are interested in the intensity-duration characteristics of heatwaves and their relationship to the circulation, we have studied four different patches of land of dimensions around 10°x10°(lat x lon), centred at around 35N, 40N, 45N and 50N (see Fig. 1, panel b). Given the general circulation of the model, these land patches span the latitudes from the eddy driven jet to the subtropical jet. In Fig. 1, the land patches are shown at different longitudinal locations for clarity; however the land patches are actually at the same longitudinal location (100°-110°). As the model is zonally symmetric (Every longitude is statistically identical), the zonal position of the land patches does not make a difference. The size of the patches are of the order of the synoptic scale (more than 1000km) to specifically study large-scale processes.

We calculate and store T_a, the daily average of the spatial average of lowest-level model temperature over the land patches of interest. The 95th percentile of the T_a distribution – T_{95} – is set to be the heatwave threshold. T_{95} is computed separately for each land patch.

Heatwave definition and characteristics

We define heatwaves as any continuous period of three or more days during which T_a exceeds T_{95} in a land patch. The duration of a heatwave is the continuous period over which T_a exceeds T_{95}. From our heatwave definition, the minimum duration possible is 3 days. Two heatwaves separated by even only a day with T_a below T_{95} are still considered as two separate events. The intensity of a heatwave is defined as the mean of the difference between T_a and T_{95} across its duration. While there are many ways in which heatwave intensity could be defined (Perkins and Alexander, 2012), we choose the average value since it is a lifetime measure of the heatwave rather than an instantaneous measure (like peak temperature for instance) which likely to be more noisy. To precisely estimate the intensity and duration of heatwaves from the daily averaged temperature data, we use linear interpolation to identify the approximate (sub-daily) times where the heatwave threshold is crossed.

For this study, we divide the heatwaves sampled into four classes - high intensity, low intensity, high duration and low duration. The high intensity and high duration classes consist of heatwaves whose respective attributes are higher than their 90th percentile values across all heatwaves. Similarly, the low intensity and low duration classes contain heatwaves whose respective attributes are lower than their 10th percentile values across all heatwaves.

Panel a of Fig. 2 shows the intensity-duration distribution for the land patch centered at 45N. Panels b and c of Fig. 2 shows how the average intensity/duration values for the top and bottom 10 percentile heatwaves change across the different land locations. We see that as we move from the northernmost land towards the equator, the average intensity values of both the top and bottom 10 percentile heatwaves decrease, by around 41% and 44% respectively.

In contrast, as we move from the northernmost land towards the equator, heatwave duration increases primarily in the positive tail of the duration distribution, with the negative tail remaining fixed. The average duration of the top 10 percentile heatwaves increases by around 28%, while the average duration of the bottom 10 percentile heatwaves does not exhibit any clear change. The relatively unchanged duration values for low duration heatwaves could be due to the 3-day minimum duration constraint, and the relative abundance of short heatwaves.

2.3 | Heatwave energetics

To study the energetics of heatwaves, we move from a framework of temperature to that of energy. We find that during heatwave days, there is a strong correlation between the average lowest-level air temperature over the area of interest and the total dry static energy (DSE) over the same horizontal area, between 970hPa and 850hPa (Fig. S1 in the supplementary material, panel a). This correlation is robust across the various land locations, and enables us to associate temperature extremes with extremes in DSE, which is a conserved quantity in the absence of diabatic sources. In all our analyses, we include one day before and after the heatwave event. This allows us to also capture the processes that push temperatures across the heatwave threshold in both directions.

We find that the sensible heat flux during heatwaves over the area of interest is mostly negative (Fig. S2 in the supplementary material), suggesting a warmer atmosphere during heatwaves, and is robust across land locations. This allows us rule out the possibility of enhanced surface fluxes being a forcing mechanism for heatwaves in this model. Conversely, this strongly suggests that the heatwaves in this model are primarily forced by the circulation, with sensible heat flux only acting as a negative response to this forcing.

Across land locations, for heatwave periods, we find that changes in the total DSE (S) between 970hPa and 850hPa can be explained to a large extent (except for a few outliers) by the DSE advection in the atmosphere (Fig. S1 in the supplementary material, panel b). We see that the linear fit is slightly steeper than the 1:1 line, with the DSE advection rate slightly overestimating the actual rate of DSE change. This bias is consistent with the fact that we have excluded the effects of radiative forcing, which act to remove DSE.

We can formulate the time-evolution of DSE (S) as

$$\frac{\partial S}{\partial t} = \left.\frac{\partial S}{\partial t}\right|_{advection} + res \tag{3}$$

DSE tendency is expressed as the sum of DSE advection and a residual term res. Note that the tendency terms are calculated at the midpoints of consecutive heatwave days, with time grids that are staggered relative to heatwave days. In all subsequent plots of DSE tendency, this time grid (at the mid-point of heatwave days) is used.

The dynamical core does not output vertical winds by default, so we calculate them from a diagnostic equation (see the supplementary material). For details on the DSE budget and advection calculations, see the appendix.

2.4 | Reynolds decomposition

To understand how the different advective components govern intensity and duration of heatwaves, we perform a Reynolds decomposition of DSE advection ($-\mathbf{u}.\nabla s$) within the area of interest, between 970hPa and 850hPa (where s is the DSE at individual grid points). We split $\mathbf{u}$ into its mean and anomaly components as $\mathbf{u} = \overline{\mathbf{u}} + \mathbf{u}'$. Similarly, we split DSE as $s = \overline{s} + s'$. Since the model has a constant forcing without diurnal or seasonal cycles, we set the mean values in the Reynolds decomposition to be the climatological values across the 1000 years that the model was run for. The total DSE advection (-$\mathbf{u}.\nabla s$) can be decomposed as

$$-\mathbf{u}.\nabla(s) = -\overline{\mathbf{u}}.\nabla(\overline{s}) - \overline{\mathbf{u}}.\nabla(s') - \mathbf{u}'.\nabla(\overline{s}) - \mathbf{u}'.\nabla(s') \tag{4}$$

Given the zonal symmetry of the model, we expect $\frac{\partial \overline{S}}{\partial x}$ to be close to zero. We also expect $\overline{v}$ to be small. Conversely, terms involving v' and $\overline{u}$ (depending on proximity to the eddy jet), could be important.

2.5 | Intensity-duration control

To partition the intensity into contributions from the different Reynolds components, we begin by noting that the total DSE tendency due to advection can be integrated over time to estimate the time evolution of DSE over the lifetime of the heatwave. The value of DSE at the start of the heatwave (close to the heatwave threshold) is taken to be zero. From this time evolution of DSE, we can compute the intensity (in Joules) as the average DSE across heatwave duration. The linear relationship between low-level DSE and lowest-level model temperature (Fig. S1 in the supplementary material) also allows us to convert intensity from Joules to Kelvin.

Given that the individual DSE advection components add upto the total DSE advection, the above approach can also be used to compute contribution of individual components of the total advection by integrating the DSE tendency due to any individual component over the heatwave lifetime and computing a DSE intensity due to this component alone. Due to the linearity of both averaging and integration, this directly partitions the total intensity into contributions due to each advection component (See Fig. 4).

To quantify the contribution of the different components to heatwave duration, we have plotted the average magnitude associated with each process on the nth day after heatwave start. (See Fig. 5). As we intend to capture the trends in the accumulation rates (same as positive DSE tendency) of various components in relation to heatwave duration, we do not normalise on duration. We compute the average accumulation rates associated with each process across heatwaves that have survived till the nth day. This enables us to understand their temporal profiles and trends with heatwave duration.

3 | RESULTS

3.1 | Low-level DSE advection

In Fig. 3, we have plotted the total DSE advection (between 970hPa and 850hPa) within the land patches centered at 50N and 35N. To compare between heatwaves of varying lengths, we have plotted against time fraction, with 0 and 1 being the first and last day across all heatwaves. As we would expect, DSE advection is initially positive, leading to an accumulation of DSE. Advection then reduces to zero (at heatwave maximum), before reversing sign. Negative DSE advection towards the end of the heatwave ventilates the accumulated DSE, ending the event.

We see from Fig. 3 that intense heatwaves are associated with a high amplitude of positive and negative DSE advection, with an almost linear profile. In contrast, high duration heatwaves have a persistent rate of accumulation, with a brief and delayed ventilation (same as negative accumulation). Interestingly, the DSE advection pattern of low intensity heatwaves looks similar to that of high duration heatwaves, and that of low duration heatwaves looks like that of high intensity heatwaves. These patterns are consistent across all land locations (Not shown). It is important to note that the amplitude of DSE advection decreases from the 50N box to the 35N box, across all heatwave classes.

This explains why the average intensity of heatwaves also decreases in the same direction.

3.2 | Reynolds components

We observe that of all the terms obtained from Reynolds decomposition at the lower levels (970hPa to 850hPa), four horizontal terms and the vertical component account for nearly all of the DSE advection. The horizontal terms are

- $-v' \frac{\partial \overline{S}}{\partial y}$ - meridional advection of mean DSE by anomalous wind
- $-v' \frac{\partial S'}{\partial y}$ - meridional advection of anomalous DSE by anomalous wind
- $-\overline{u} \frac{\partial S'}{\partial x}$ - zonal advection of anomalous DSE by mean wind
- $-u' \frac{\partial S'}{\partial x}$ - zonal advection of anomalous DSE by anomalous wind

Fig. S3 in the supplementary material shows the lifetime profiles reconstructed from the four horizontal terms and the vertical term, and are almost indistinguishable from the total lifetime DSE advection profiles in Fig. 3. The aggregate lifetime profiles of the individual components across heatwave classes for the 50N and 35N land locations are also plotted (see Figs. S4-7 in the supplementary material)

We see that most components look very similar across land locations and heatwave class, both in their magnitude and profile. The only component that systematically changes in magnitude across land locations is the $\overline{u} \frac{\partial S'}{\partial x}$ component, which decreases sharply as we move equatorward, away from the surface westerlies. This suggests that the $\overline{u} \frac{\partial S'}{\partial x}$ term in particular might be responsible for the trends in mean intensity-duration of heatwaves, atleast across land locations. The differences in $-v' \frac{\partial \overline{S}}{\partial y}$ and $-v' \frac{\partial S'}{\partial y}$ across land locations is relatively small and of opposite signs, such that their sum ($-v' \frac{\partial S}{\partial y}$) changes little between land locations. The difference in $-v' \frac{\partial \overline{S}}{\partial y}$ term across land locations can be explained by the slight change in climatological DSE gradient with latitude (See Fig. S8 in the supplementary material).

3.3 | Contribution to Intensity

In Fig. 4, we have plotted the intensity contributions associated with different processes for the top and bottom 10 percentile intensity classes, respectively. For completeness, we have also computed the residual term as the deviation between the actual DSE difference and DSE advection (As in Fig. S1 in the supplementary material). This term includes processes that we have not accounted for like surface fluxes and radiation forcing, along with averaging-related errors.

We have converted quantities in these plots from Joules to Kelvin using the linear relationship between low-level DSE and lowest-level model temperature (see Fig. S1 in the supplementary material). Note that the mean total intensities we have calculated from the DSE advection in Fig. 4 are in close agreement with their corresponding values in Fig. 2 (indicated as a shaded range over the boxes on the left in Fig. 4).

In subsequent analyses, we have combined the $v' \frac{\partial \overline{S}}{\partial y}$ and $v' \frac{\partial S'}{\partial y}$ terms as $v' \frac{\partial\ S}{\partial y}$. The $v' \frac{\partial \overline{S}}{\partial y}$ term is predominantly accumulating and the $v' \frac{\partial S'}{\partial y}$ is ventilating (See Figs. S4 and S5 in the supplementary material). The combination of these terms ($v' \frac{\partial\ S}{\partial y}$) explains trends in heatwave characteristics better than either term individually.

Fig. 4 highlights the components responsible for the difference in mean intensity between the top and bottom intensity classes, and between extreme land locations. Between the top and bottom intensity classes, the component that shows the most systematic change in intensity contribution is $v' \frac{\partial S}{\partial y}$. Between extreme land locations however, the $\overline{u} \frac{\partial S'}{\partial x}$ term has the most significant difference in contribution, with the magnitude of the $\overline{u} \frac{\partial S'}{\partial x}$ dropping sharply as we move away from the jet.

The residual term shows some differences between intensity classes and land locations. However, the trends in the residual term is always opposed to that of intensity and in all cases, the residual term only contributes negatively to heatwave intensity. This observation is in agreement with our understanding that the processes in the residual term only act to dampen heatwaves. Furthermore, given its small amplitude relative to the dominant advection terms, we expect that it plays a small role in determining the intensity characteristics of heatwaves in our model.

3.4 | Contribution to Duration

The duration of heatwaves is considered to be the time taken for the DSE to rise above and fall below its threshold value. This requires the initial accumulation of DSE (initiating the heatwave) followed by ventilation of DSE (dissipating the heatwave).

We have plotted the average accumulation rates associated with different components across the duration of the event. We have plotted this separately for the top and bottom 10 percentile duration classes for the extreme land locations (Fig. 5). Figs. S9-10 in the supplementary material shows the individual components along with their variability across heatwaves.

The most systematic difference between the top and bottom duration classes is the number of days before ventilation starts. In the top duration class, ventilation starts after around 6 days, whereas it only takes about 1.5 days in the bottom duration class. Another difference is the ventilation provided by the $v' \frac{\partial S}{\partial y}$ term. The $v' \frac{\partial S}{\partial y}$ term contributes to ventilation in the bottom duration class, leading to a shorter duration of heatwaves. For the top duration class, this term provides relatively negligible ventilation.

The primary ventilation term is different between extreme land locations. Close to the jet, ventilation follows the $\overline{u} \frac{\partial S'}{\partial x}$ term, and away from the jet, it follows the $u' \frac{\partial S'}{\partial x}$ term. These processes have different ventilation rates, with $\overline{u} \frac{\partial S'}{\partial x}$ being stronger than $u' \frac{\partial S'}{\partial x}$. Given that the accumulation periods are almost the same across extreme land locations, the duration trend across land locations can be attributed to the change in the ventilation time due to the difference in ventilation rates between the $\overline{u} \frac{\partial S'}{\partial x}$ and $u' \frac{\partial S'}{\partial x}$ terms. The fact that $\overline{u}$ close to the jet stream has a constant direction and is generally of higher magnitude than u', which varies in both direction and magnitude with time might explain why $\overline{u} \frac{\partial S'}{\partial x}$ provide more ventilation than $u' \frac{\partial S'}{\partial x}$ on average.

We can estimate heatwave duration from the total accumulation profiles in Fig. 5 by first dividing the profile into accumulation and ventilation phases, and then calculating the ventilation time that would be needed to balance the total accumulation. Heatwave duration can be calculated as the sum of the number of days of accumulation and the ratio of total accumulation to mean ventilation. The duration estimate from this calculation (not shown) agrees very well with the corresponding values and trends in Fig. 2.

In most cases, the residual term opposes DSE advection. In all cases, the magnitude of this term is small and does not change the results much.

3.5 | Synoptic-scale circulation

To investigate the particular circulation conditions that lead to intense and long heatwaves, we look at composites of heatwaves with intensity and duration in the top 2 percentile (around 30 heatwaves each). Figs. S11-14 in the supplementary material show the total winds averaged between 950 hPa and 850 hPa for the top 2 percentile intense and long heatwaves at 50N and 35N. We see that heatwaves in our model are caused by anti-cyclonic systems that are positioned towards the east of the land patch, with their poleward-directed flank over the box. The meridional wind advects warm air from closer to the equator, which leads to DSE accumulation. The ventilation is then carried out by the zonal wind, advecting the warm air out of the box.

Given that the circulation patterns that lead to heatwaves in our model is roughly baroclinic and homogeneous (Fig. S15 in the supplementary material, with the advection terms following their corresponding DSE gradient), we can explain the behaviour of the advection terms using the wind and DSE gradient profiles. In Fig. 6, we have plotted the patch-averaged profiles of the anomalous DSE gradient terms ($\frac{\partial S'}{\partial x}$ and $\frac{\partial S'}{\partial y}$) along with the wind terms (v' and $\overline{u}/u'$ depending on the location of the land patch) for the top 2 percentile intense and long heatwaves at 50N and 35N.

From Fig. 6, we see that heatwaves are initiated by the anomalous meridional wind v' ($\overline{v}$ is close to zero), advecting the climatological meridional DSE gradient $\frac{\partial \overline{S}}{\partial y}$. The profile of $\frac{\partial S'}{\partial y}$ follows v' across land locations and heatwave characteristic. During heatwaves, v' advects DSE into the box, homogenising the DSE inside the box (See Figs. S16-19 in the supplementary material), leading to a positive $\frac{\partial S'}{\partial y}$ (the climatological gradient $\frac{\partial \overline{S}}{\partial y}$ is negative). $\frac{\partial S'}{\partial x}$ is roughly anti-correlated to $\frac{\partial S'}{\partial x}$, with $\frac{\partial S'}{\partial x}$ increasing as $\frac{\partial S'}{\partial x}$ decreases. The $\overline{u}/u'$ wind ($\overline{u}$ at 50N, u' at 35N) is positive across heatwave lifetime.

Long duration heatwaves seem to be associated with weaker DSE anomalies, zonal DSE gradients and winds that have a smaller zonal component as observed in Fig. 6 and Figs. S11-14. This combination of DSE gradients and winds can be achieved by a weak, slowly moving (or stationary) anticyclone. The two peaks in v' observed in Fig. 6b,d also suggest that long duration heatwaves may occur due to multiple anticyclones passing over the region during the heatwave, or that a quasi-stationary anticyclone may be re-energized by downstream propagation of energy. Shorter heatwaves are associated with additional ventilation by the meridional term as seen in Fig. 5c,d , suggesting that a cyclone likely followed the anticyclone that led to the heatwave.

For intense heatwaves in both land patches, we observe that $\frac{\partial S'}{\partial y}$ starts at a small value at the beginning of the heatwave, reaches a maximum and then reduces to a small value by the end of the heatwave. $\frac{\partial S'}{\partial x}$ is strongly negative at the beginning suggesting that the DSE anomaly is primarily developing at the western edge of the box. It goes to zero near the peak of the $\frac{\partial S'}{\partial y}$ anomaly and becomes positive, leading to ventilation. This evolution is consistent with the picture of a high amplitude, isolated eddy entering and exiting the land patches. This is supported by the composites in Figs. S16-17, where the location of maximum v' moves west to east over the box as the heatwave progresses, with the DSE anomaly having a sharp tongue like shape.

For long duration heatwaves, we observe that $\frac{\partial S'}{\partial y}$ is at or close to its peak value, suggesting that a "preconditioning" of the DSE gradient has occurred. This preconditioning also keeps $\frac{\partial S'}{\partial x}$ at a small value, and the termination of the heatwave seems to be similar to what is observed in the high intensity case. This is supported by the composites in Figs. S18-19 , where the DSE anomaly is much broader to the west of the box (particularly in panel b of Figs. S18-19, a third into the heatwave), rendering the zonal accumulation/ventilation small (due to small $\frac{\partial S'}{\partial x}$) until the termination of the heatwave.

3.6 | Relation to the large scale circulation

In the previous few sections, we have looked at the contributions of the individual advection components to the intensity and duration of individual heatwaves, and used composites to understand the circulation patterns associated with these contributions. The next step is to connect these contributions to the general circulation of the model.

From a one-dimensional stirring perspective, we might expect that latitudes with higher variance of meridional winds might often experience larger deformation of DSE contours, leading to a higher mean intensity for heatwaves at that latitude – this follows from the fact that extremes are more sensitive to the scale parameter as compared to the location parameter (Katz and Brown, 1992). The meridional DSE gradient does not vary much between the different land patches (see Fig. S8 in the supplementary material), and the typical magnitude of the meridional winds can be inferred from the variance of the meridional winds. As we have seen in Fig. 1d, the variance of near-surface meridional winds maximizes near 50N and declines as we move equatorward, which might be a reasonable explanation for the intensity trend. However, such reasoning only holds in the case of no eddy-eddy interactions, and recent idealised studies have shown that the nonlinear meridional term $v' \frac{\partial S'}{\partial y}$ works to dampen the quasilinear term (Garfinkel and Harnik, 2016; Linz et al., 2018). In fact, Linz et al. (2018) shows that the variance of the advected temperature (analogous to DSE in our case) has a much flatter meridional distribution even if the stirring is centered at a single latitude. Therefore, consistent with predictions in Linz et al. (2018) from a much simpler model, we see in Fig. 4 that the contribution of $v' \frac{\partial S}{\partial y}$ in both extreme land patches is similar, and the primary difference is due to the $\overline{u} \frac{\partial S'}{\partial x}$.

Coming to the question of heatwave duration, Fig. 5 shows that the zonal contribution is primarily in ventilating the accumulated DSE, though the meridional contribution plays a role in determining short vs. long heatwaves in the same latitude. In regions of climatological surface westerlies (see Fig. 1c), this ventilation is more effective due to the stronger zonal winds, whereas this ventilation has to be achieved by the eddy zonal winds associated with the synoptic system (or an eddy that passes the region subsequently). Keeping in mind that the ventilation depends not only on the zonal wind magnitude but also on $\frac{\partial S'}{\partial x}$, we observe that regions with high meridional wind variance are also associated with stronger gradients of $\frac{\partial S'}{\partial x}$ (Supplementary Fig. S22). Why this should be the case is unclear, and likely has to do with of scalar mixing by a turbulent flow. Therefore, we expect that heatwaves occurring away from regions of surface westerlies are likely to last longer. Furthermore, since surface westerlies are induced to remove the momentum convergence by upper tropospheric eddies (Held, 2007), regions of high meridional wind variance (and $\frac{\partial S'}{\partial x}$ variance) coincide with regions of high zonal winds – this is true in both hemispheres as seen in Fig. 1d, providing a clear explanation why intensity-duration characteristics of heatwaves are likely to be inversely related if heatwaves are primarily governed by the atmospheric circulation.

4 | SUMMARY AND DISCUSSION

In this study, we use an idealised GCM to understand how the large-scale circulation impacts the statistics of temperature extremes. To achieve this, we used the following approach:

1. We used a GCM configuration that minimizes/eliminates diabatic forcing of temperature extremes, so that it is easier to understand the impacts of the circulation.
2. We used the tight relationship between lower-tropospheric DSE and near-surface temperatures in the model to transform the problem from that of temperature extremes to lower-tropospheric DSE extremes. We chose to do this because DSE is conserved by atmospheric flows and allows for unambiguous attribution to individual Reynolds decomposed components of the atmospheric flow.
3. The choice of using DSE made it possible to use the conservation law to create a quantitative framework to partition flow contributions to the intensity and duration of heatwaves. This is advantageous since it does not require mechanism denial type approaches which can alter the flow itself (see Arblaster et al., 2014; Wehrli et al., 2019; Miralles et al., 2014, for example), making it problematic to perform quantitative attribution.
4. Once we identify flow components that quantitatively contribute to the intensity/duration characteristics, we try to relate the statistics of these components to features of the large-scale circulation such as the location of storm tracks, variance of meridional winds and surface westerlies.

Due to the above methodological approach, we were able to not only quantify the contribution of the circulation to the intensity-duration characteristics of individual heatwaves, but were able to explain how the *statistics*, particularly the mean, of heatwave intensity and duration are related to the large scale circulation. Linking the statistics of extreme events to the large-scale circulation remains an outstanding challenge for the community (see White et al., 2022, for example), and our work contributes to this effort.

We show that the mean heatwave intensity and duration are strongly influenced by the eddy wind terms and the location of the eddy driven jet, which are closely linked to the storm tracks. The location and intensity of storm tracks varies seasonally, with a stronger and more equatorward storm track in the winter (Shaw et al., 2016). Moreover, the poleward shift of the storm tracks is a robust signal observed under climate change scenarios, especially for the southern hemisphere (Barnes and Polvani, 2013). These trends are even simulated and captured in idealised dry models (Tandon et al., 2011; Butler et al., 2010). Given the variability and the expected changes in the storm track location with warming, this study contributes to understanding how the statistics of heatwave characteristics could be modified as a consequence.

We observe that meridional advection is important to distinguish between high and low intensity/duration in a single latitude. However, it is the zonal advection term that plays a primary role in distinguishing between high intensity/duration heatwaves across latitudes. The role of zonal advection has generally not received much attention in the literature concerned with the shape of temperature PDFs (Schneider et al., 2014; Garfinkel and Harnik, 2016; Tamarin-Brodsky et al., 2019), likely because they were concerned with PDFs along an entire latitude belt and not in a single location; Recent observational work focusing on a single location does show that zonal advection plays an important role (Shah and Monteiro, submitted). Given the importance of zonal advection, a potential question of interest is what controls the statistics of $\frac{\partial S'}{\partial x}$, particularly its mean and variance.

Our work also contributes to understanding the effect of nonlinear advection on temperature variability. Even though quasilinear models of atmospheric macroturbulence – which ignore eddy-eddy interactions – have been successful in recovering flow statistics in a variety of geophysical flows (particularly in regions with a strong mean flow) (Schneider and Walker, 2006; Chemke and Kaspi, 2016; Delsole and Farrell, 1996; Marston and Tobias, 2023; Svirsky et al., 2023a,b), more recent work has shown that nonlinear advection is important to generate the skewness that is present in the observed temperature distribution (Garfinkel and Harnik, 2016; Tamarin-Brodsky et al., 2019). In this context, our results suggest that quasilinear models are unlikely to reproduce the tail behaviour of temperature variability, and this conclusion is supported by recent observational work as well (Shah and Monteiro, submitted).

A limitation of our study is the absence of surface forcing and zonal inhomogeneities (which might lead to stationary waves), both of which are likely to impact extreme events (Miralles et al., 2014; Narinesingh et al., 2020), and it remains to be seen if the DSE framework developed in the current work can be extended to such situations. Since we also account for a residual term, this framework could also incorporate surface and radiative fluxes, and a similar approach shows promise in understanding temperature variability in observational data as well (Shah and Monteiro, submitted).

code availability

The analysis code is available at `https://github.com/Ai33L/Heatwave_dyn1`

data availability

The data that support the findings of this study are available from the corresponding author upon reasonable request.

acknowledgements

The support and the resources provided by 'PARAM Brahma Facility' under the National Supercomputing Mission, Government of India at the Indian Institute of Science Education and Research (IISER) Pune are gratefully acknowledged. JMM acknowledges useful discussions with Nili Harnik and Rodrigo Caballero which helped frame the manuscript better. A.S thanks Sarathchandran J. for technical help with the supercomputer code and Koh Kawaguchi for suggestions that have greatly improved the figures in this paper.

conflict of interest

The authors declare no conflict of interest.

Appendix A. DSE budgeting

Consider a 10°x10° box bounded at at 970hPa at the bottom, and 850hPa at the top. The DSE (s) at each point in the box is computed as

$$s = c_p T + gz \tag{5}$$

where c_p=1004.64 J kg^{-1} K^{-1} is the specific heat of air at constant pressure, T is temperature, g= 9.80665 ms^{-2} is acceleration due to gravity, and z is height above the surface. The total DSE (S) in the box is then given by

$$S = \int_V \left(\frac{c_p T}{g} + z \right) dV \tag{6}$$

Where dV is a volume element in pressure coordinates. S can change either due to adiabatic processes (advection), or by diabatic processes (radiation or latent heat release from convection).

$$\frac{\partial S}{\partial t} = \left.\frac{\partial S}{\partial t}\right|_{adiabatic} + \left.\frac{\partial S}{\partial t}\right|_{diabatic} \tag{7}$$

Focusing on DSE tendency from adiabatic processes,

$$\left.\frac{\partial S}{\partial t}\right|_{adiabatic} = \left.\frac{\partial S}{\partial t}\right|_{advection} = -\int_A \left(\frac{s\mathbf{u}}{g} \right) . \mathbf{dA} \tag{8}$$

where **dA** is an area element on the box surface, and with the vertical axis in pressure coordinates. Since DSE is conserved along the flow, S cannot be changed by rearrangement of air parcels within the box. DSE tendency due to circulation must pass through one of the surfaces of the box.

In the presence of diabatic terms, DSE tendency is then

$$\frac{\partial S}{\partial t} = -\int_A \left(\frac{\mathbf{u}s}{g}\right) . \mathbf{dA} + \frac{\partial \mathbf{S}}{\partial \mathbf{t}}\bigg|_{\mathbf{diabatic}} \tag{9}$$

Hence, in the absence of diabatic sources and flux of DSE across a box surface, the DSE in the box cannot change. Adiabatic DSE tendency can alternatively be expressed as a volume integral of DSE advection in pressure coordinates

$$\frac{\partial S}{\partial t}\bigg|_{adiabatic} = -\int_V \left(\frac{\mathbf{u}.\nabla s}{g}\right) dV \tag{10}$$

Appendix B. DSE advection calculation

The DSE and DSE advection are computed in the area of interest for heatwave periods using the daily-averaged model variables. The model variables are first linearly interpolated to uniform pressure levels spanning from 970hPa to 290hPa, at 20hPa intervals. The highest pressure level for interpolation is set to 970hPa as some grid points have close to 970hPa at the lowest model level. DSE and DSE advection are then calculated at each grid point and volume integrated in pressure coordinates.

The total DSE (S) within the box is computed for each heatwave day as

$$S = \sum_N (c_p T_N + z_N g)\, dx_N dy_N \frac{dp_N}{g} \tag{11}$$

where N iterates over all the grids in the box. T_N is the temperature, z_N is the height, and dx_N, dy_N and dp_N are the dimension lengths associated with each grid point.

The advection terms are calculated on a staggered time grid (between consecutive heatwave days). The DSE advection between two consecutive days $d1$ and $d2$ is calculated as the average of the DSE advection on the two days.

$$\frac{\partial S}{\partial t}|_{advection} = -\frac{1}{2}\sum_{d1,d2}\sum_N (\mathbf{u_N}.\nabla(c_p T_N + z_N g))\, dx_N dy_N \frac{dp_N}{g} \tag{12}$$

The gradient terms are calculated by performing spatial centered-finite differencing. The Reynolds decomposed advection terms are also calculated in the same manner.

references

Arblaster, J. M., Lim, E.-P., Hendon, H. H., Trewin, B. C., Wheeler, M. C., Liu, G. and Braganza, K. (2014) Understanding Australia's hottest September on record.

Barnes, E. A. and Polvani, L. (2013) Response of the Midlatitude Jets, and of Their Variability, to Increased Greenhouse Gases in the CMIP5 Models. URL: `https://journals.ametsoc.org/view/journals/clim/26/18/jcli-d-12-00536.1.xml`.

Barriopedro, D., García-Herrera, R., Ordóñez, C., Miralles, D. G. and Salcedo-Sanz, S. (2023) Heat Waves: Physical Understanding and Scientific Challenges. *Reviews of Geophysics*, **61**, e2022RG000780. URL: https://onlinelibrary.wiley.com/doi/abs/10.1029/2022RG000780.

Butler, A. H., Thompson, D. W. J. and Heikes, R. (2010) The Steady-State Atmospheric Circulation Response to Climate Change–like Thermal Forcings in a Simple General Circulation Model. URL: https://journals.ametsoc.org/view/journals/clim/23/13/2010jcli3228.1.xml.

Chemke, R. and Kaspi, Y. (2016) The Effect of Eddy–Eddy Interactions on Jet Formation and Macroturbulent Scales. *Journal of the Atmospheric Sciences*, **73**, 2049–2059. URL: https://journals.ametsoc.org/view/journals/atsc/73/5/jas-d-15-0375.1.xml. Publisher: American Meteorological Society Section: Journal of the Atmospheric Sciences.

Delsole, T. and Farrell, B. F. (1996) The Quasi-Linear Equilibration of a Thermally Maintained, Stochastically Excited Jet in a Quasigeostrophic Model. *Journal of the Atmospheric Sciences*, **53**, 1781–1797. URL: https://journals.ametsoc.org/view/journals/atsc/53/13/1520-0469_1996_053_1781_tqleoa_2_0_co_2.xml. Publisher: American Meteorological Society Section: Journal of the Atmospheric Sciences.

Domeisen, D. I. V., Eltahir, E. A. B., Fischer, E. M., Knutti, R., Perkins-Kirkpatrick, S. E., Schär, C., Seneviratne, S. I., Weisheimer, A. and Wernli, H. (2022) Prediction and projection of heatwaves. *Nature Reviews Earth & Environment*, **4**, 36–50. URL: https://www.nature.com/articles/s43017-022-00371-z.

Emanuel, K. A. and Živković Rothman, M. (1999) Development and Evaluation of a Convection Scheme for Use in Climate Models. *Journal of the Atmospheric Sciences*, **56**, 1766–1782. URL: http://journals.ametsoc.org.ezp.sub.su.se/doi/abs/10.1175/1520-0469(1999)056%3C1766%3ADAEOAC%3E2.0.CO%3B2. 00553.

Frierson, D. M. W., Held, I. M. and Zurita-Gotor, P. (2006) A Gray-Radiation Aquaplanet Moist GCM. Part I: Static Stability and Eddy Scale. *Journal of the Atmospheric Sciences*, **63**, 2548–2566. URL: http://journals.ametsoc.org/doi/abs/10.1175/JAS3753.1.

Garfinkel, C. I. and Harnik, N. (2016) The Non-Gaussianity and Spatial Asymmetry of Temperature Extremes Relative to the Storm Track: The Role of Horizontal Advection. *Journal of Climate*, **30**, 445–464. URL: https://journals.ametsoc.org/doi/10.1175/JCLI-D-15-0806.1.

Heifetz, E., Bishop, C. H., Hoskins, B. J. and Methven, J. (2004) The counter-propagating Rossby-wave perspective on baroclinic instability. I: Mathematical basis. *Quarterly Journal of the Royal Meteorological Society*, **130**, 211–231. URL: https://onlinelibrary.wiley.com/doi/abs/10.1002/qj.200413059610.

Held, I. M. (2007) *Progress and problems in large-scale atmospheric dynamics*. Princeton University Press. URL: http://www.asp.ucar.edu/thompson/2005/pdf/final_withfigs.pdf.

Hoskins, B. J., McIntyre, M. E. and Robertson, A. W. (1985) On the use and significance of isentropic potential vorticity maps. *Quarterly Journal of the Royal Meteorological Society*, **111**, 877–946. URL: http://rmets.onlinelibrary.wiley.com/doi/abs/10.1002/qj.49711147002.

Jiménez-Esteve, B., Kornhuber, K. and Domeisen, D. I. V. (2022) Heat Extremes Driven by Amplification of Phase-Locked Circumglobal Waves Forced by Topography in an Idealized Atmospheric Model. *Geophysical Research Letters*, **49**, e2021GL096337. URL: https://onlinelibrary.wiley.com/doi/abs/10.1029/2021GL096337. _eprint: https://onlinelibrary.wiley.com/doi/pdf/10.1029/2021GL096337.

Jiménez-Esteve, B. and Domeisen, D. I. (2022) The role of atmospheric dynamics and large-scale topography in driving heatwaves. *Quarterly Journal of the Royal Meteorological Society*, **148**, 2344–2367. URL: https://rmets.onlinelibrary.wiley.com/doi/10.1002/qj.4306.

Katz, R. W. and Brown, B. G. (1992) Extreme events in a changing climate: Variability is more important than averages. **21**, 289–302. URL: https://doi.org/10.1007/BF00139728.

Lee, S. and Kim, H.-k. (2003) The Dynamical Relationship between Subtropical and Eddy-Driven Jets. *Journal of the Atmospheric Sciences*, **60**, 1490–1503. URL: https://journals.ametsoc.org/view/journals/atsc/60/12/1520-0469_2003_060_1490_tdrbsa_2.0.co_2.xml.

Linz, M., Chen, G. and Hu, Z. (2018) Large-Scale Atmospheric Control on Non-Gaussian Tails of Midlatitude Temperature Distributions. *Geophysical Research Letters*, **45**, 9141–9149. URL: https://agupubs.onlinelibrary.wiley.com/doi/abs/10.1029/2018GL079324.

Marston, J. B. and Tobias, S. M. (2023) Recent Developments in Theories of Inhomogeneous and Anisotropic Turbulence. *Annual Review of Fluid Mechanics*, **55**, 351–375. URL: https://www.annualreviews.org/content/journals/10.1146/annurev-fluid-120720-031006. Publisher: Annual Reviews.

Miralles, D. G., Teuling, A. J., van Heerwaarden, C. C. and Vilà-Guerau de Arellano, J. (2014) Mega-heatwave temperatures due to combined soil desiccation and atmospheric heat accumulation. *Nature Geoscience*, **7**, 345–349. URL: https://www.nature.com/articles/ngeo2141. Publisher: Nature Publishing Group.

Monteiro, J. M., McGibbon, J. and Caballero, R. (2018) sympl (v. 0.4.0) and climt (v. 0.15.3) – towards a flexible framework for building model hierarchies in Python. *Geoscientific Model Development*, **11**, 3781–3794. URL: https://www.geosci-model-dev.net/11/3781/2018/.

Narinesingh, V., Booth, J. F., Clark, S. K. and Ming, Y. (2020) Atmospheric blocking in an aquaplanet and the impact of orography. **1**, 293–311. URL: https://wcd.copernicus.org/articles/1/293/2020/.

Perkins, S. E. (2015) A review on the scientific understanding of heatwaves—Their measurement, driving mechanisms, and changes at the global scale. *Atmospheric Research*, **164-165**, 242–267. URL: https://www.sciencedirect.com/science/article/pii/S0169809515001738.

Perkins, S. E. and Alexander, L. V. (2012) On the Measurement of Heat Waves. *Journal of Climate*, **26**, 4500–4517. URL: https://journals.ametsoc.org/doi/abs/10.1175/JCLI-D-12-00383.1.

Röthlisberger, M. and Papritz, L. (2023) Quantifying the physical processes leading to atmospheric hot extremes at a global scale. *Nature Geoscience*, **16**, 210–216. URL: https://www.nature.com/articles/s41561-023-01126-1.

Schneider, T., Bischoff, T. and Płotka, H. (2014) Physics of Changes in Synoptic Midlatitude Temperature Variability. *Journal of Climate*, **28**, 2312–2331. URL: http://journals.ametsoc.org/doi/abs/10.1175/JCLI-D-14-00632.1.

Schneider, T. and Walker, C. C. (2006) Self-Organization of Atmospheric Macroturbulence into Critical States of Weak Nonlinear Eddy–Eddy Interactions. *Journal of the Atmospheric Sciences*, **63**, 1569–1586. URL: http://journals.ametsoc.org/doi/abs/10.1175/jas3699.1.

Shah, H. M. and Monteiro, J. M. (submitted) The role of synoptic circulations in lower-tropospheric DSE variability over a South Asian heatwave hotspot. URL: https://www.authorea.com/doi/full/10.22541/essoar.174349794.49450607?commit=4cea58bef2f3c3172fe26803a8031b5fe5008c9b.

Shaw, T. A., Baldwin, M., Barnes, E. A., Caballero, R., Garfinkel, C. I., Hwang, Y.-T., Li, C., O'Gorman, P. A., Rivière, G., Simpson, I. R. and Voigt, A. (2016) Storm track processes and the opposing influences of climate change. **9**, 656–664. URL: https://www.nature.com/articles/ngeo2783.

Svirsky, A., Herbert, C. and Frishman, A. (2023a) Statistics of inhomogeneous turbulence in large-scale quasigeostrophic dynamics. *Physical Review E*, **108**, 065102. URL: https://link.aps.org/doi/10.1103/PhysRevE.108.065102.

— (2023b) Two-Dimensional Turbulence with Local Interactions: Statistics of the Condensate. *Physical Review Letters*, **131**, 224003. URL: https://link.aps.org/doi/10.1103/PhysRevLett.131.224003.

Tamarin-Brodsky, T., Hodges, K., Hoskins, B. J. and Shepherd, T. G. (2019) A Dynamical Perspective on Atmospheric Temperature Variability and Its Response to Climate Change. *Journal of Climate*, **32**, 1707–1724. URL: https://journals.ametsoc.org/doi/full/10.1175/JCLI-D-18-0462.1.

Tandon, N. F., Polvani, L. M. and Davis, S. M. (2011) The Response of the Tropospheric Circulation to Water Vapor–Like Forcings in the Stratosphere. URL: https://journals.ametsoc.org/view/journals/clim/24/21/jcli-d-11-00069.1.xml.

Wehrli, K., Guillod, B. P., Hauser, M., Leclair, M. and Seneviratne, S. I. (2019) Identifying Key Driving Processes of Major Recent Heat Waves. *Journal of Geophysical Research: Atmospheres*, **124**, 11746–11765. URL: https://onlinelibrary.wiley.com/doi/abs/10.1029/2019JD030635. _eprint: https://onlinelibrary.wiley.com/doi/pdf/10.1029/2019JD030635.

White, R. H., Kornhuber, K., Martius, O. and Wirth, V. (2022) From Atmospheric Waves to Heatwaves: A Waveguide Perspective for Understanding and Predicting Concurrent, Persistent, and Extreme Extratropical Weather. **103**, E923–E935. URL: https://journals.ametsoc.org/view/journals/bams/103/3/BAMS-D-21-0170.1.xml.

List of Figures

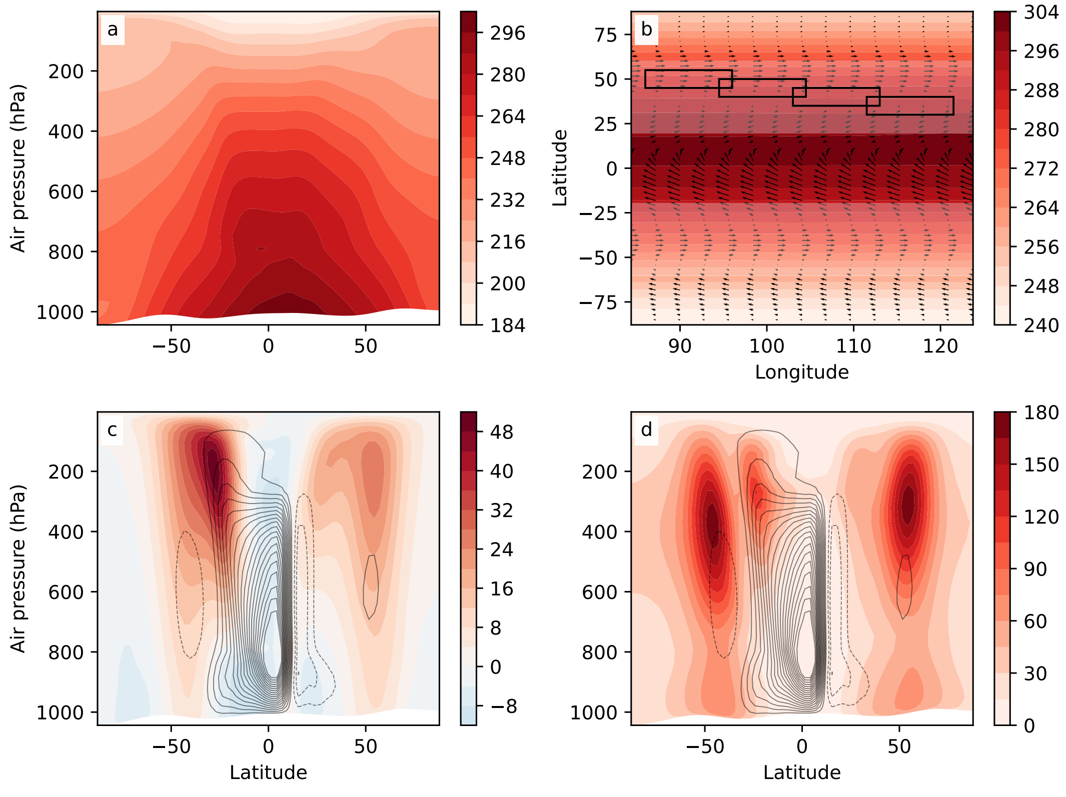

FIGURE 1 Model climatology. (a) Zonally averaged air temperature (K). (b) Lowest level winds (ms^{-1}) overlaid on lowest level air-temperature (K). The location and extent of land in the model is depicted by the light shading, and the land patches of interest are depicted by solid boxes. All land patches are between 100-110 longitude, boxes in the plot have been separated for clarity. (c) Zonally averaged zonal winds (ms^{-1}, coloured) overlaid with the zonal mean meridional mass streamfunction (contours; solid for positive, dashed for negative and zero removed; contour interval $2x10^{10}$ kgs^{-1}) (d) Zonal mean variance of meridional wind (m^2s^{-2}) - marks the location of the storm track. The zonal mean meridional mass streamfunction is overlaid (black contours, as in panel c).

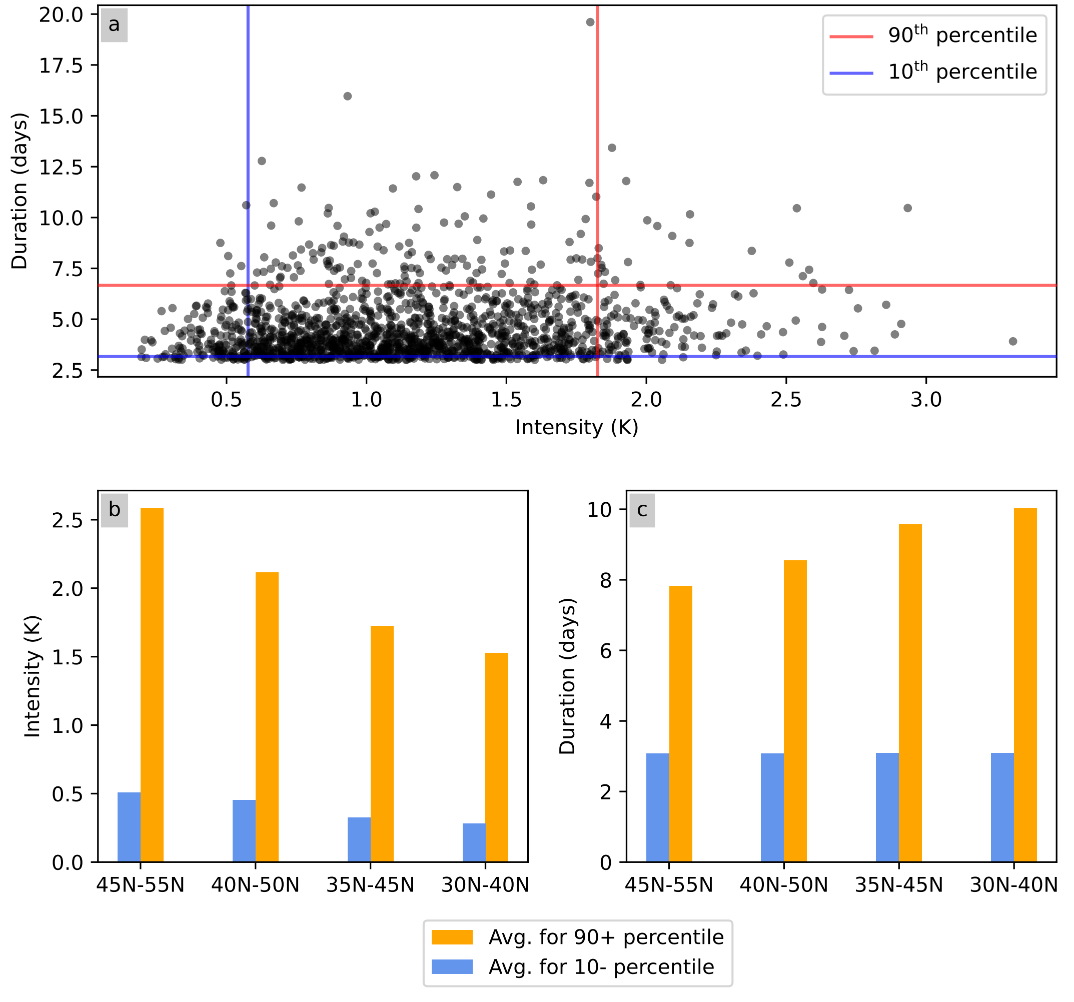

FIGURE 2 (a) Scatter plot of heatwave intensity-duration for land patch centered at 45N. The red and blue lines indicate the 90 and 10 percentile thresholds for both intensity and duration. Average (b) intensity values and (c) duration values for the lowest and highest 10 percentile heatwaves across land locations.

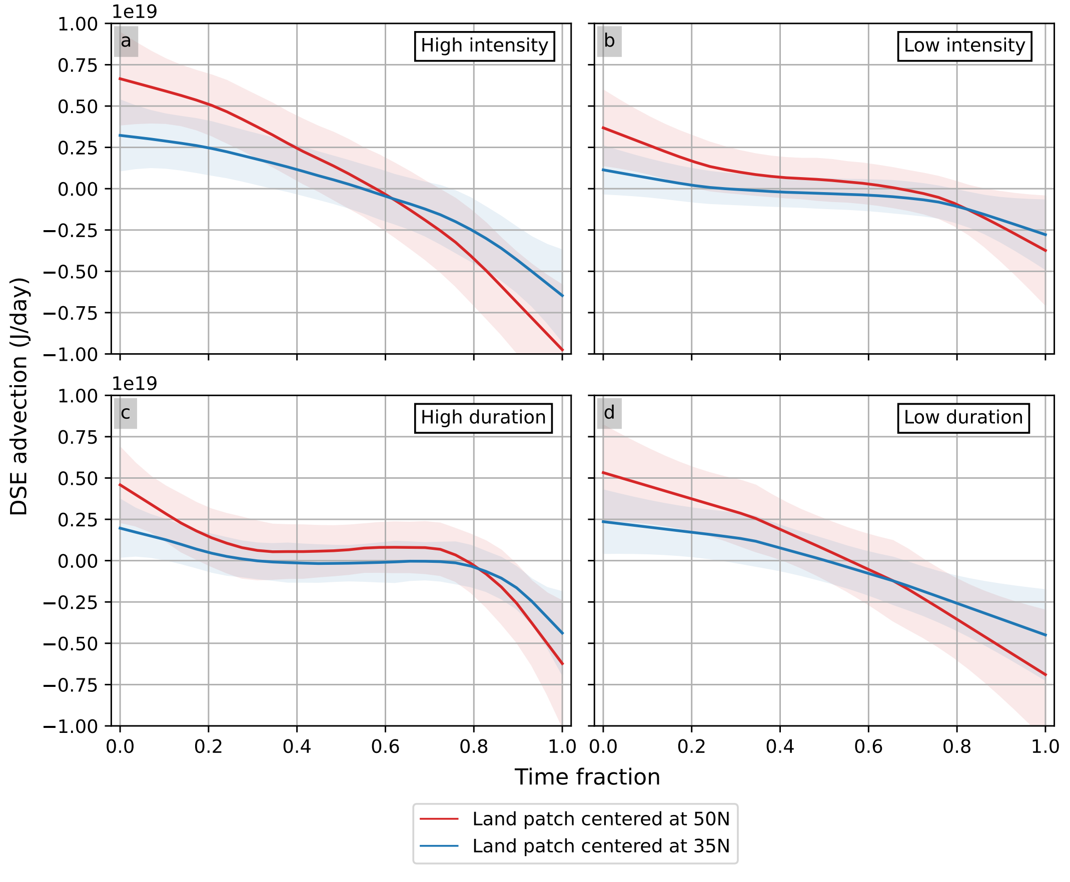

FIGURE 3 Total low-level (970hPa - 850hPa) DSE advection profiles for the different intensity and duration classes. To compare between heatwaves of varying lengths, we have plotted against time fraction, with 0 and 1 being the first and last day across heatwaves. The lines represent the mean, and shading shows standard deviation across heatwaves in each class.

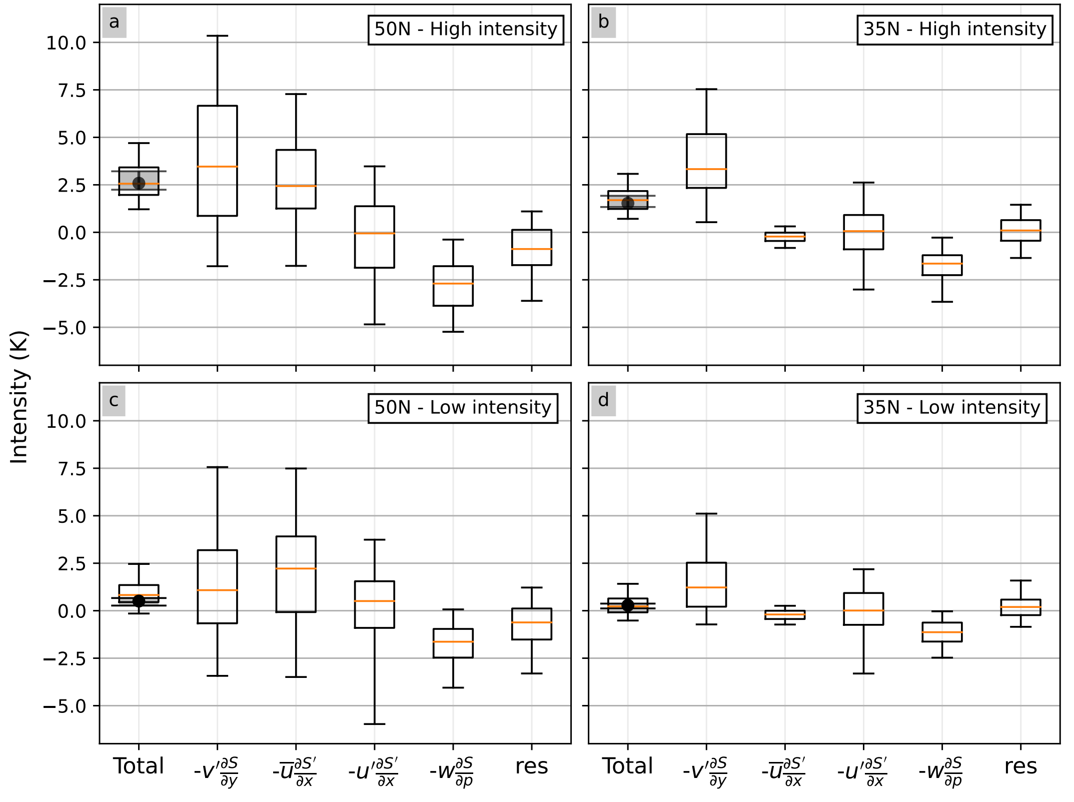

FIGURE 4 Intensity contribution of the different components for top and bottom 10 percentile intense heatwaves. The box spans from 25 to 75 percentile, and the whiskers are 5 and 95 percentile. res is the residual term. The shaded range overlaid on the total intensity box shows the intensity values of the corresponding heatwave class calculated from temperature (as in Fig. 2). The shaded region spans from the 5th to the 90th percentile of intensity values, with the mean intensity shown by the black dot.

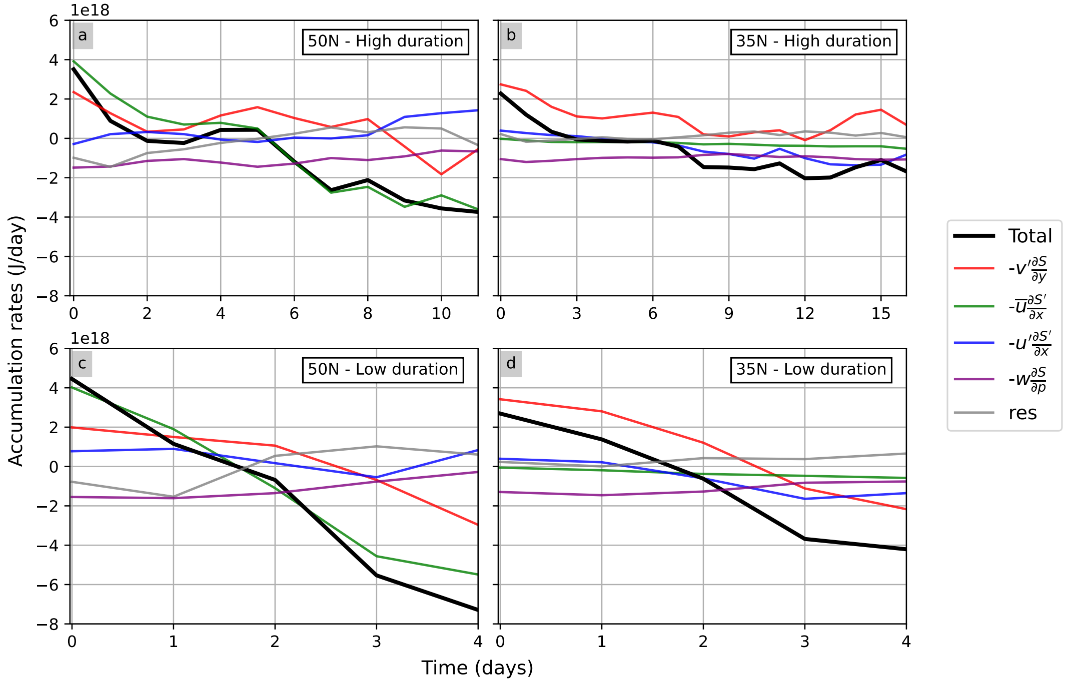

FIGURE 5 Mean accumulation rates associated with major components on the nth day after heatwave start for the top and bottom 10 percentile duration heatwaves. The profiles only include heatwaves that survive till the nth day after heatwave start. The advection components are calculated at the midpoints of consecutive heatwave days, resulting in a time grid staggered relative to heatwave days.

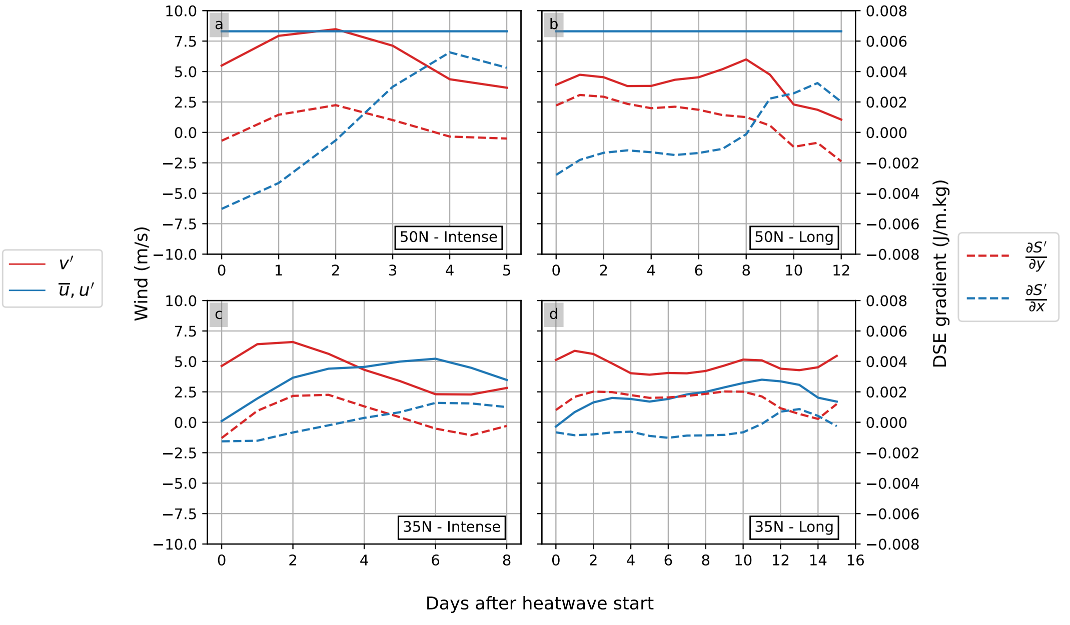

FIGURE 6 Patch-average profiles of v', $\overline{u}/u'$ ($\overline{u}$ at 50N, u' at 35N), $\frac{\partial S'}{\partial y}$ and $\frac{\partial S'}{\partial x}$ for the top 2 percentile intense and long heatwaves at 50N and 35N. The profiles only include heatwaves that survive till the nth day after heatwave start. These quantities are calculated at the midpoints of consecutive heatwave days, resulting in a time grid staggered relative to heatwave days.

Supplementary material

Abel Shibu[1] and Joy Monteiro[2,3]

[1]Department of Physics, Imperial College London, London SW7 2AZ, United Kingdom
[2]Department of Earth and Climate Science, Indian Institute of Science Education and Research Pune, Pune, India
[3]Department of Data Science, Indian Institute of Science Education and Research Pune, Pune, India

Vertical wind computation

The vertical wind w is diagnosed as

$$w = -\int_{o}^{\eta} \nabla . \left(v_H \frac{\partial p}{\partial \eta} \right) d\eta + \vec{v_H} . \nabla p \tag{1}$$

where η is the σ-p hybrid coordinate defined on model levels as

$$\eta = \frac{A(\eta) - p_{top}}{p_s - p_{top}} + B(\eta) \tag{2}$$

$A(\eta)$ and $B(\eta)$ are calculated by default and available from the model at model levels. p_s is the air pressure at the surface and p_{top} is that at the top of the model.

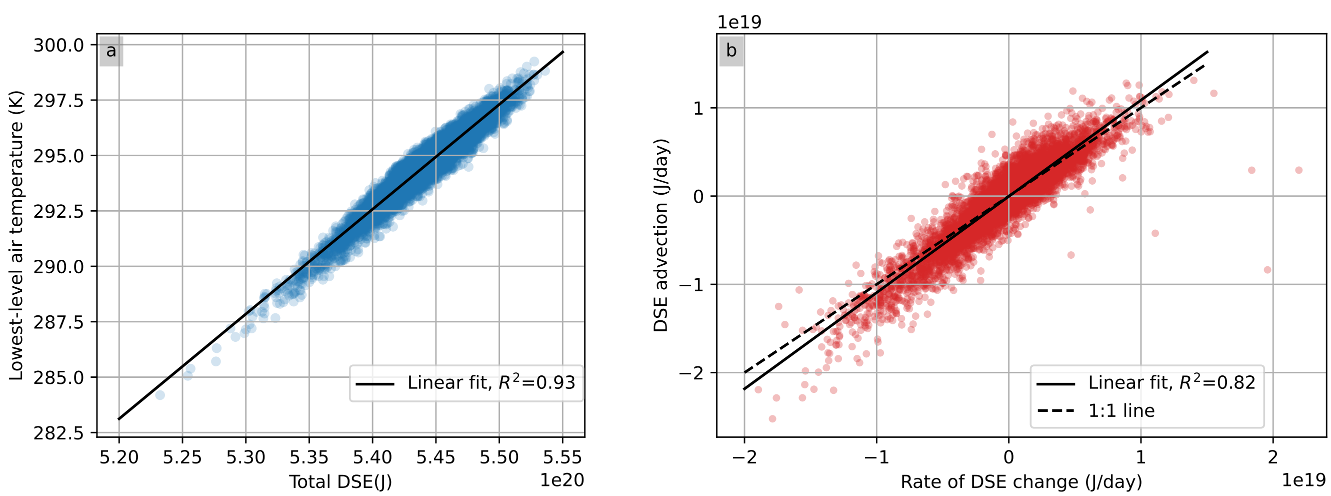

FIGURE S1: (a) Correlation between spatially-averaged lowest-level air temperature and total DSE between 970hPa and 850hPa for the land centered at 45N. The blue dots are individual heatwave days and the black line is a linear fit. (b) Comparison between rate of DSE change and the rate of DSE advection during heatwave periods for the land centered at 45N. The slope of the linear fit in panel b is 1.09.

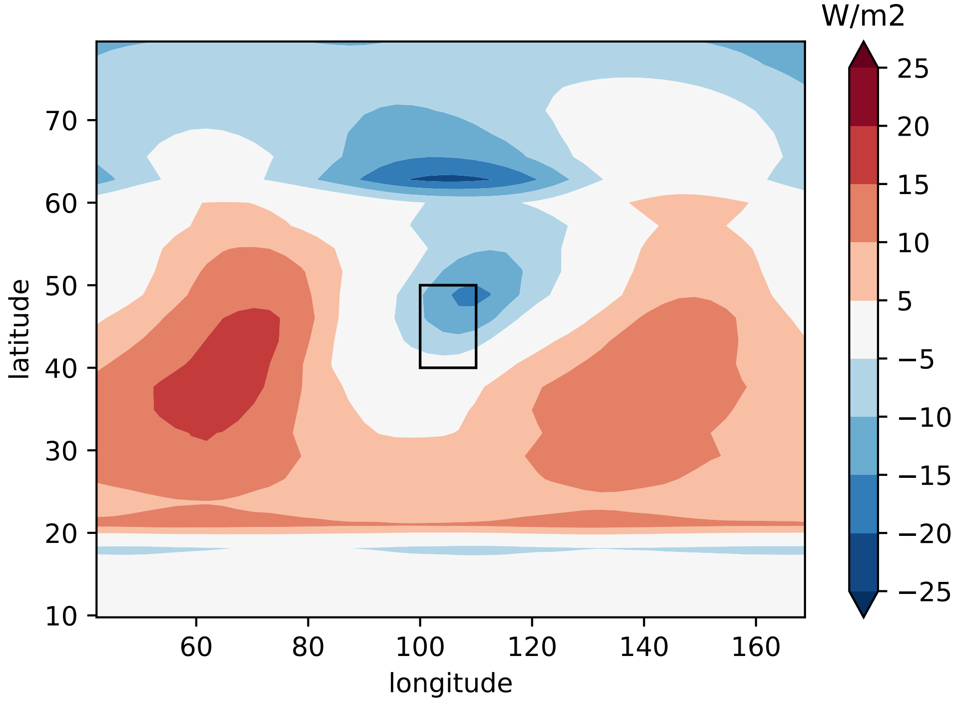

FIGURE S2: Composite of sensible heat flux anomaly at the mid-point of heatwave duration for the land patch centered at 45N.

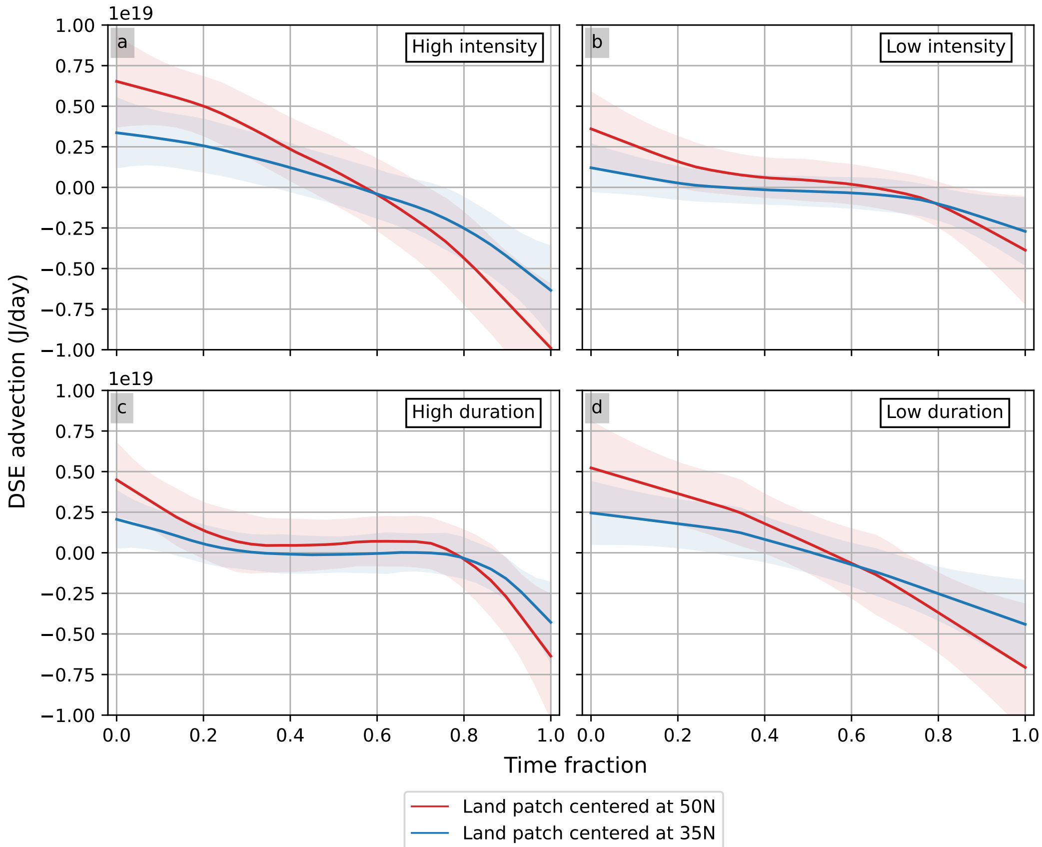

FIGURE S3: Low-level (970hPa - 850hPa) DSE advection profiles for the different intensity and duration classes reconstructed from only the four horizontal ($v'\frac{\partial \overline{S}}{\partial y}$, $v'\frac{\partial S'}{\partial y}$, $\overline{u}\frac{\partial S'}{\partial x}$ and $u'\frac{\partial S'}{\partial x}$), and the vertical component. To compare between heatwaves of varying lengths, we have plotted against time fraction, with 0 and 1 being the first and last day across heatwaves. The lines represent the mean, and shading shows standard deviation across heatwaves of each class.

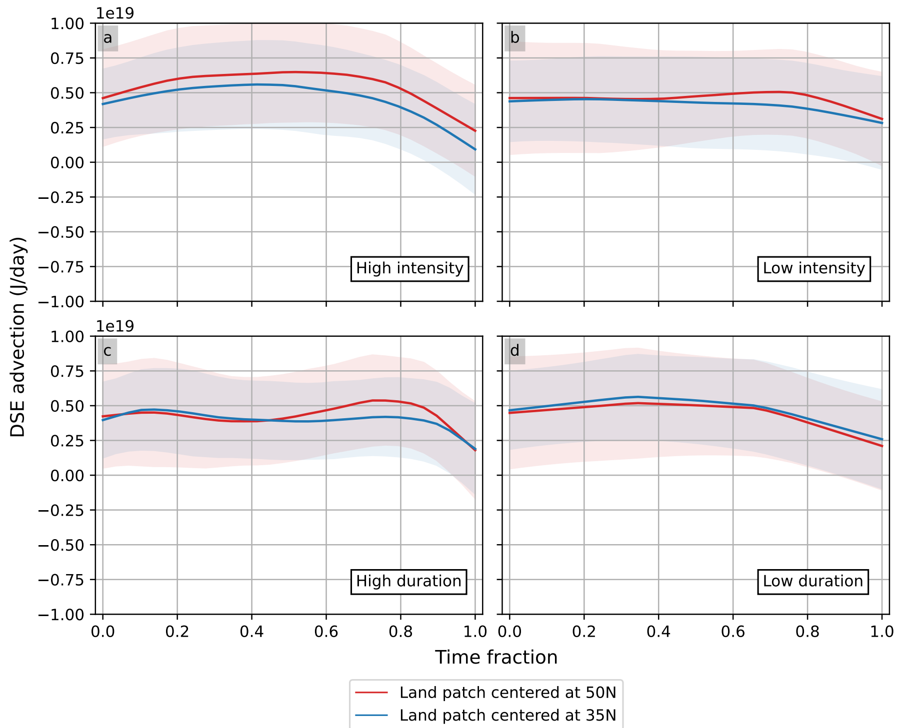

FIGURE S4: Advection profiles of $v' \frac{\partial \overline{S}}{\partial y}$ for the different heatwaves classes at 50N and 35N. These are plotted against time fraction, with 0 and 1 being the first and last day across heatwaves. The lines represent the mean, and shading shows standard deviation across heatwaves in each class.

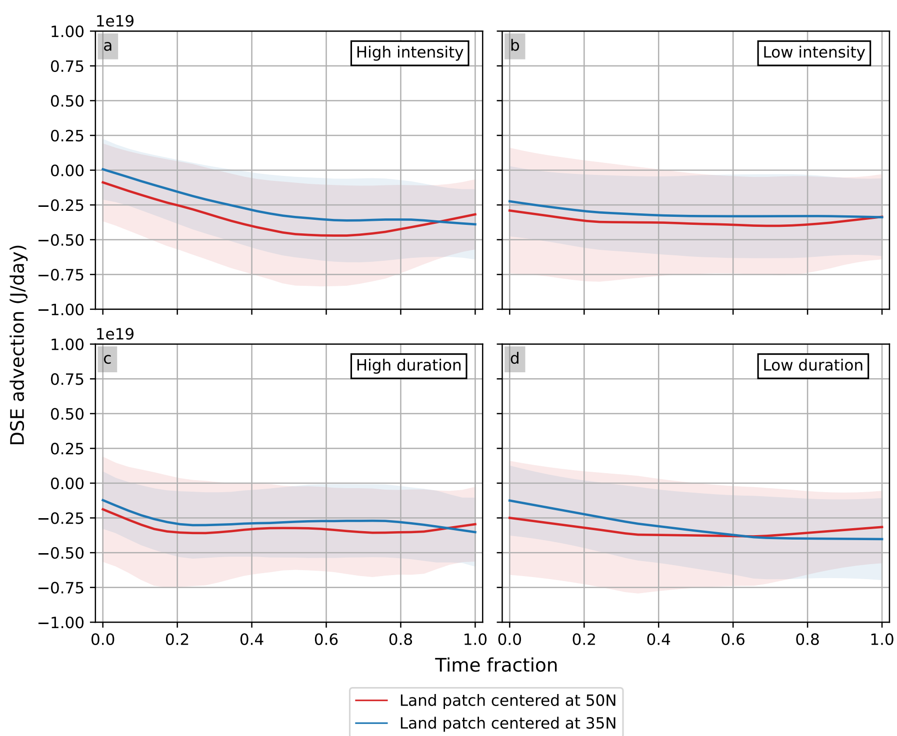

FIGURE S5: Advection profiles of $v' \frac{\partial S'}{\partial y}$ for the different heatwaves classes at 50N and 35N. These are plotted against time fraction, with 0 and 1 being the first and last day across heatwaves. The lines represent the mean, and shading shows standard deviation across heatwaves in each class.

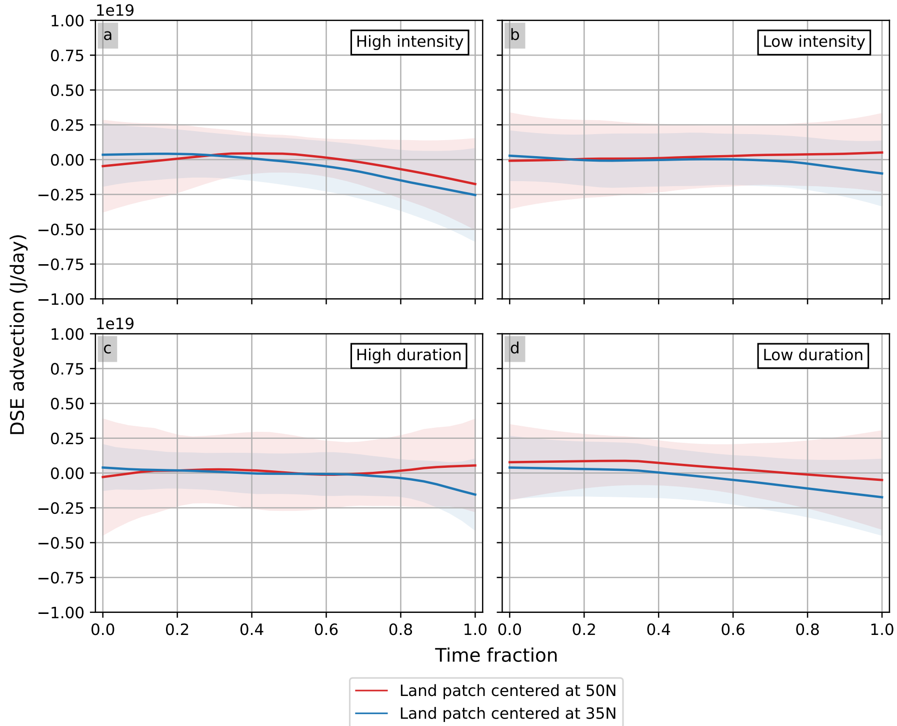

FIGURE S6: Advection profiles of $u' \frac{\partial S'}{\partial x}$ for the different heatwaves classes at 50N and 35N. These are plotted against time fraction, with 0 and 1 being the first and last day across heatwaves. The lines represent the mean, and shading shows standard deviation across heatwaves in each class.

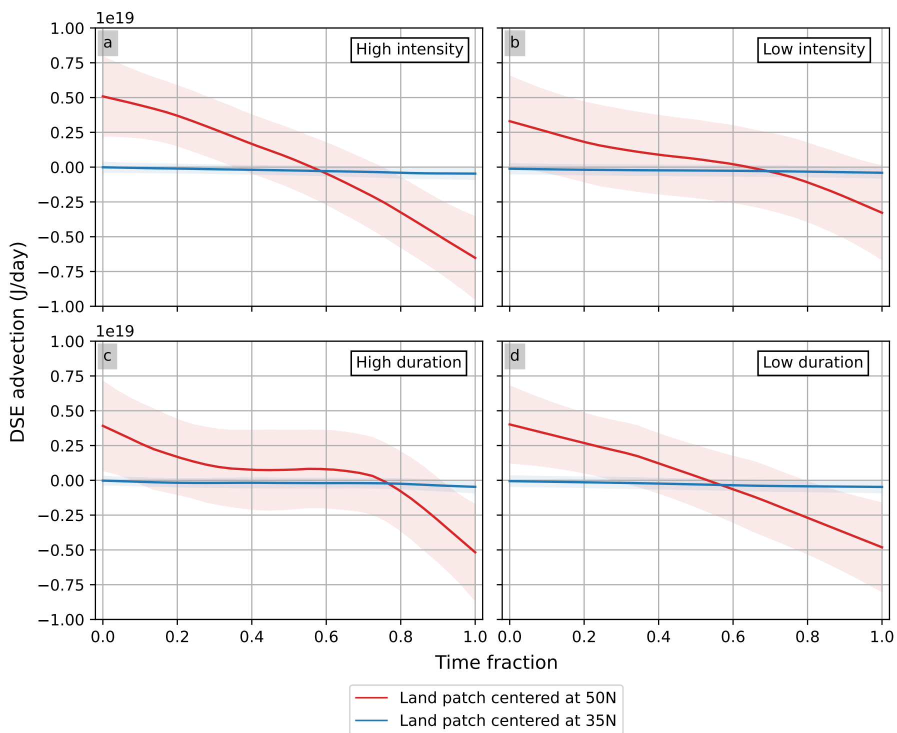

FIGURE S7: Advection profiles of $\overline{u} \frac{\partial S'}{\partial x}$ for the different heatwaves classes at 50N and 35N. These are plotted against time fraction, with 0 and 1 being the first and last day across heatwaves. The lines represent the mean, and shading shows standard deviation across heatwaves in each class.

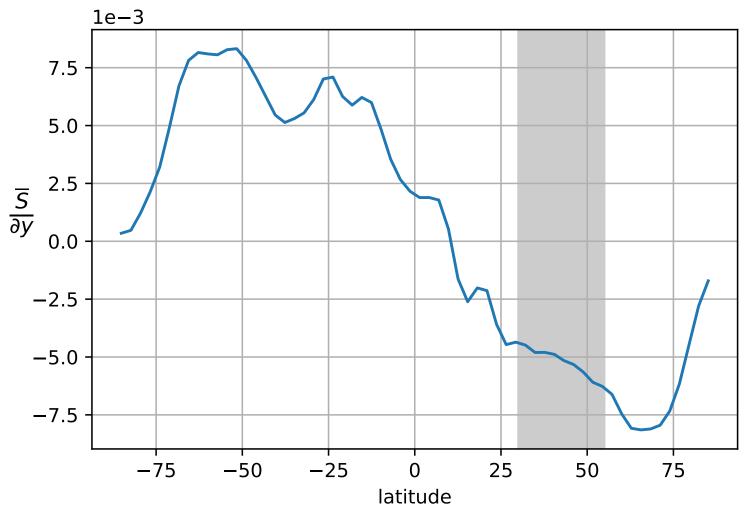

FIGURE S8: Meridional climatological DSE gradient. The DSE gradient does not change much across the regions of interest, shown by the grey shading.

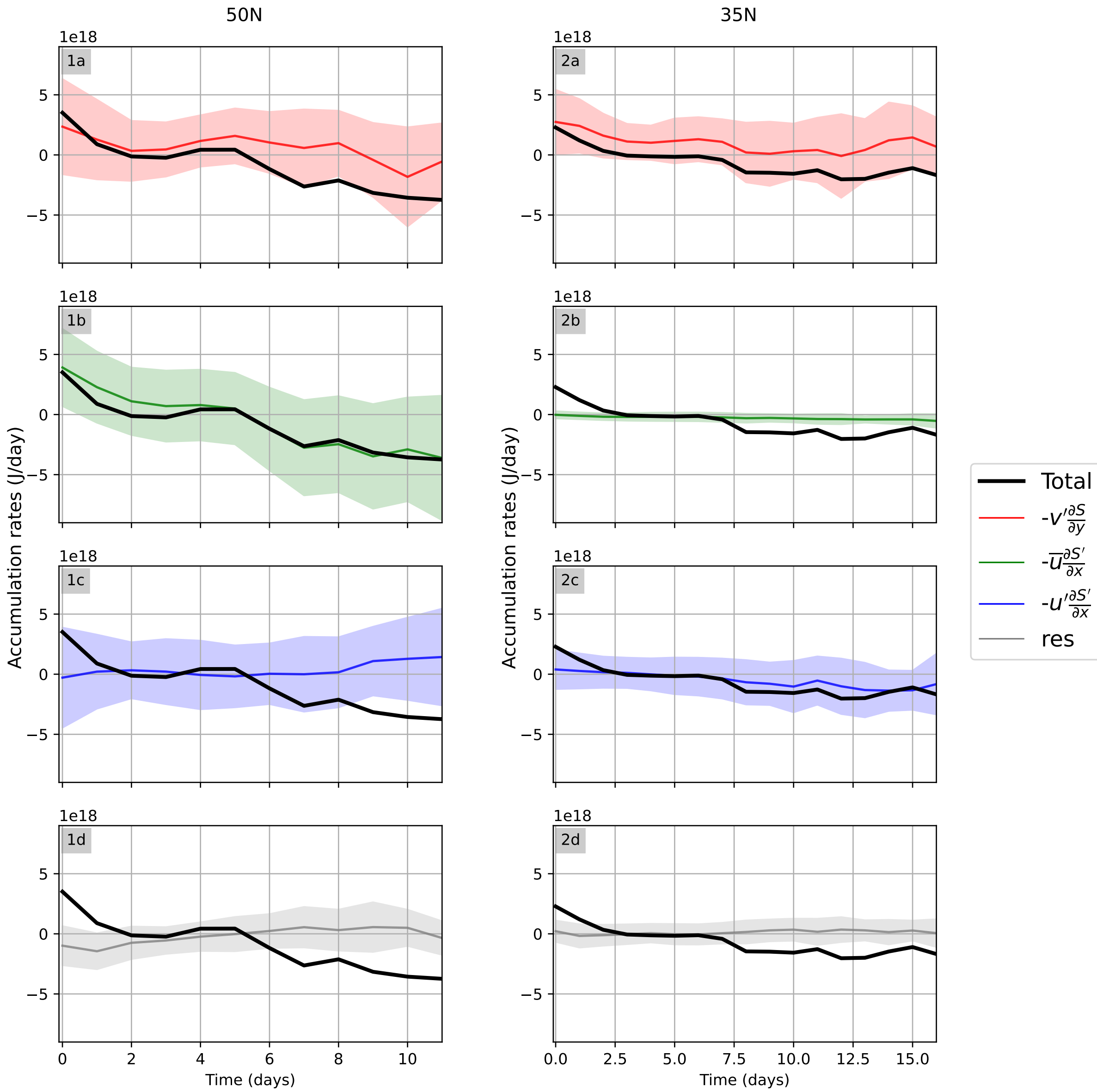

FIGURE S9: Top 10 percentile duration heatwaves. Accumulation rates associated with major components on the nth day after heatwave start. The coloured solid lines are the mean profiles and the shading indicate standard deviation. (1a-1d) 50N box. (2a-2d) 35N box.

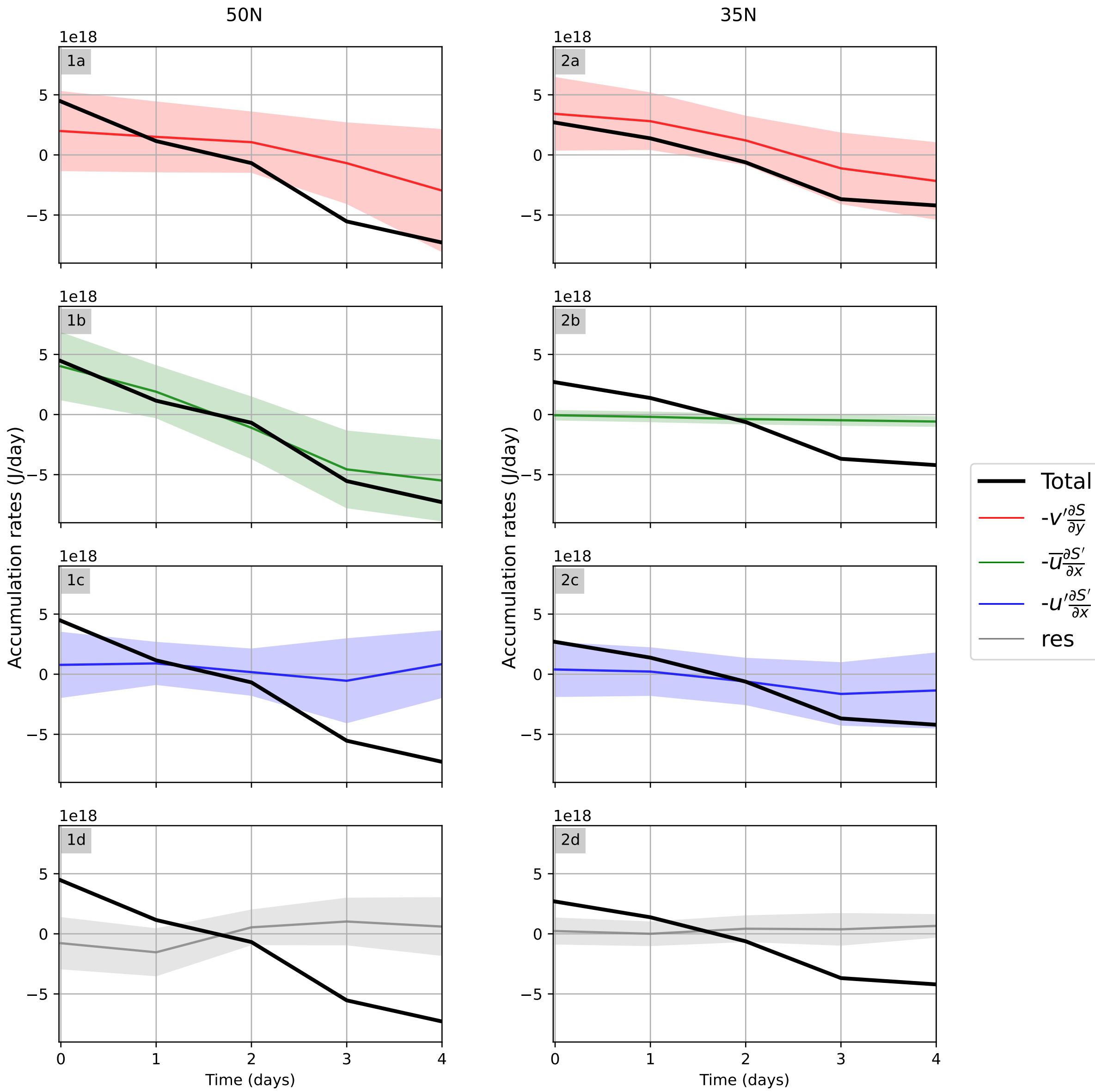

FIGURE S10: Bottom 10 percentile duration heatwaves. Accumulation rates associated with major components on the nth day after heatwave start. The coloured solid lines are the mean profiles and the shading indicate standard deviation. (1a-1d) 50N box. (2a-2d) 35N box.

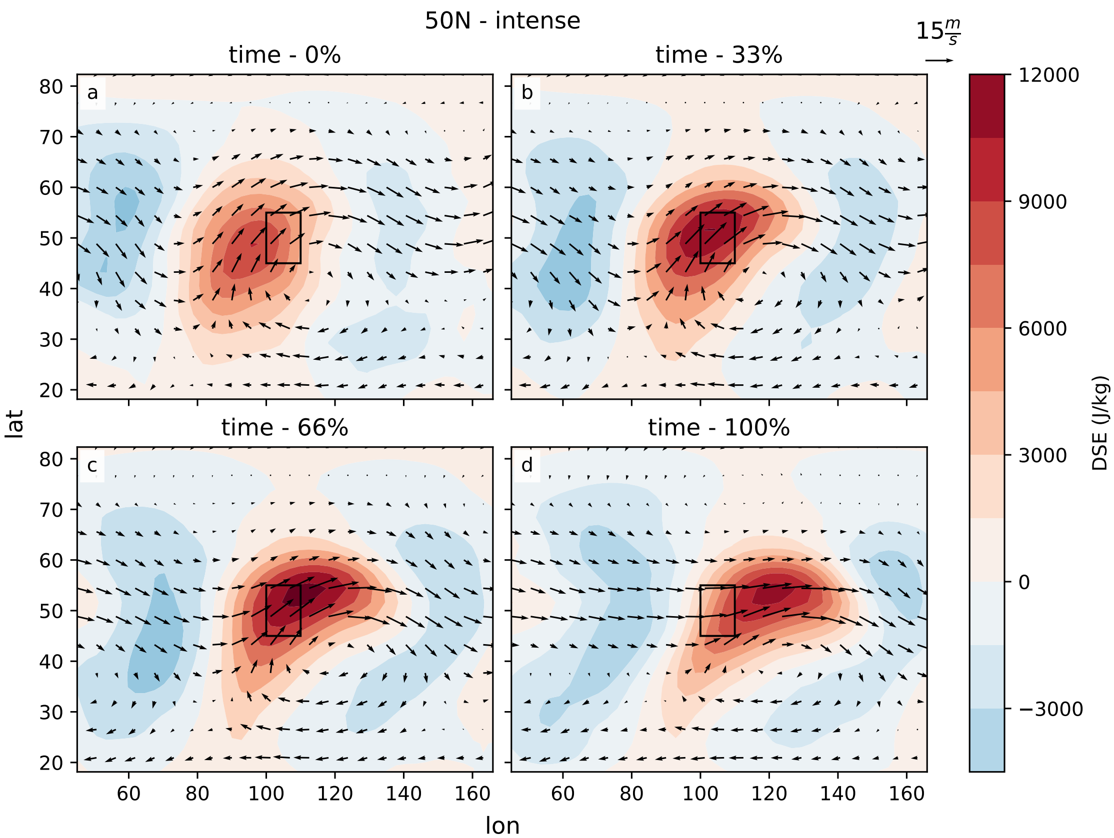

FIGURE S11: Intense heatwaves at 50N. The quivers show the total instantaneous winds averaged between 950hPa and 850hPa and the contours depict the anomalous DSE between the same levels. The plots are drawn at equal time percentage intervals, with the duration of each heatwave in the composite normalised to be between 0% and 100%.

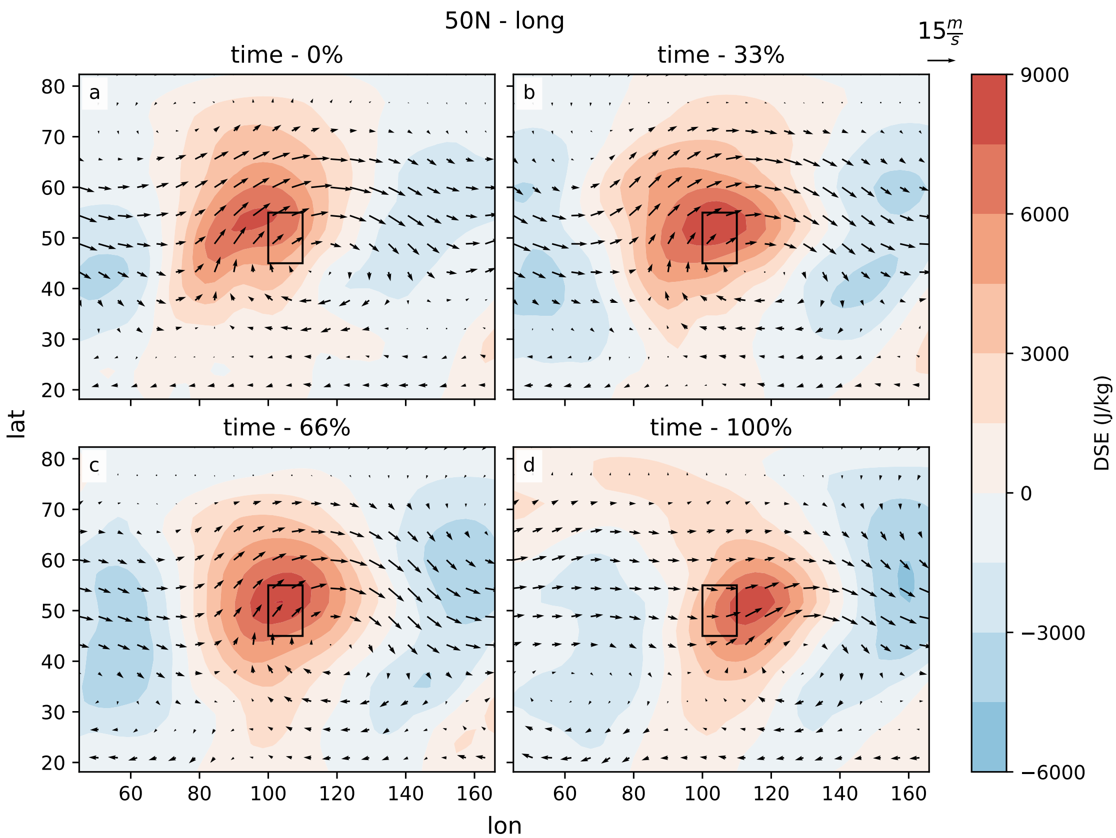

FIGURE S12: Long heatwaves at 50N. The quivers show the total instantaneous winds averaged between 950hPa and 850hPa and the contours depict the anomalous DSE between the same levels. The plots are drawn at equal time percentage intervals, with the duration of each heatwave in the composite normalised to be between 0% and 100%.

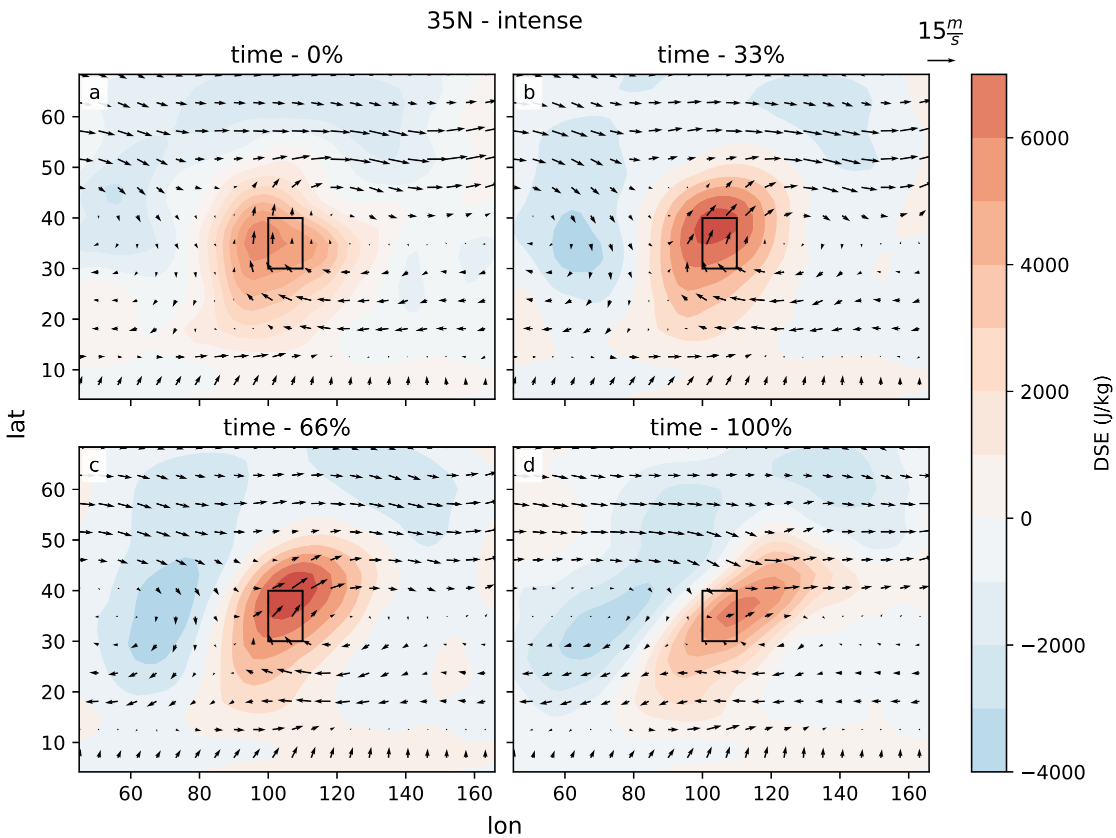

FIGURE S13: Intense heatwaves at 35N. The quivers show the total instantaneous winds averaged between 950hPa and 850hPa and the contours depict the anomalous DSE between the same levels. The plots are drawn at equal time percentage intervals, with the duration of each heatwave in the composite normalised to be between 0% and 100%.

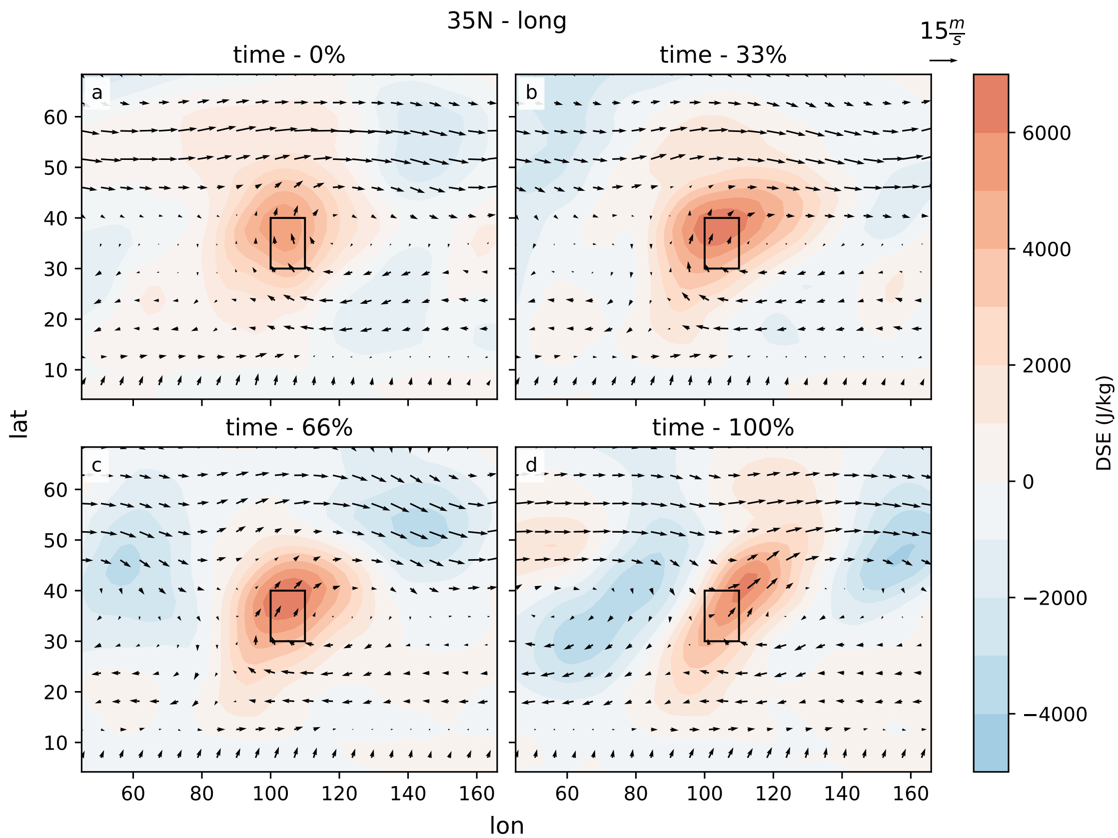

FIGURE S14: Long heatwaves at 35N. The quivers show the total instantaneous winds averaged between 950hPa and 850hPa and the contours depict the anomalous DSE between the same levels. The plots are drawn at equal time percentage intervals, with the duration of each heatwave in the composite normalised to be between 0% and 100%.

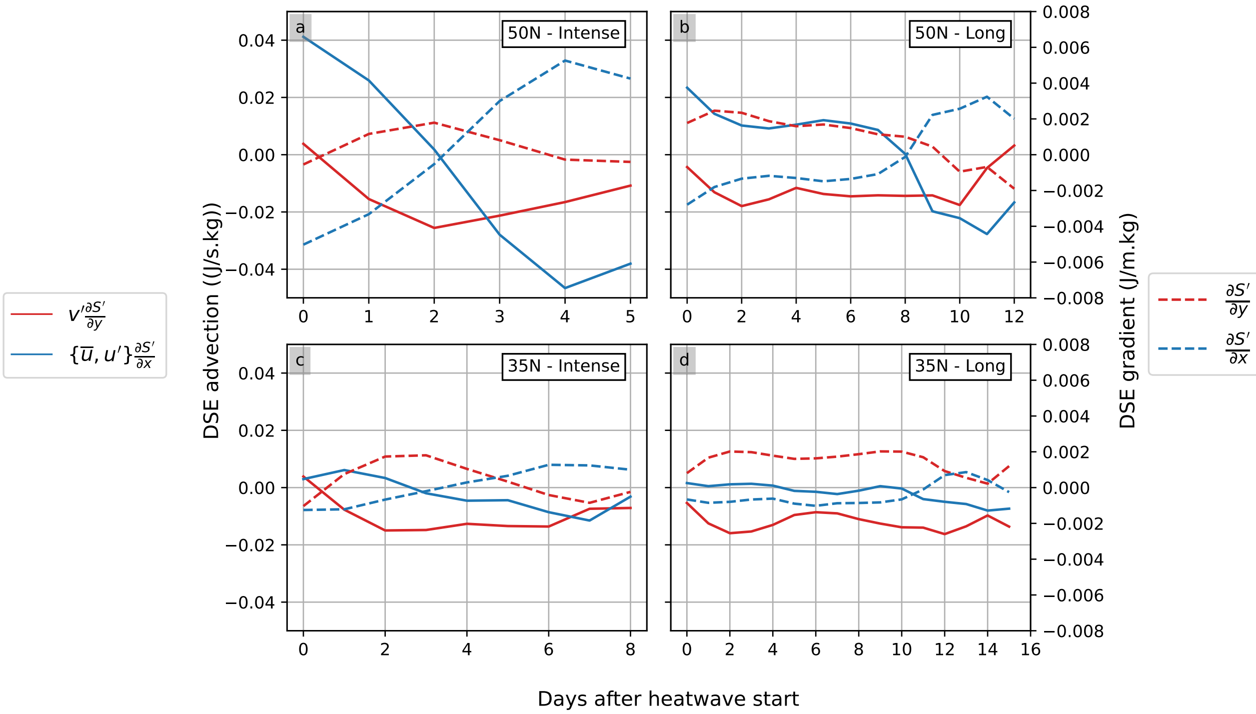

FIGURE S15: Patch-average profiles of $v'\frac{\partial S'}{\partial y}$, $\{\overline{u}/u'\}\frac{\partial S'}{\partial x}$ ($\overline{u}$ at 50N, u' at 35N), $\frac{\partial S'}{\partial y}$ and $\frac{\partial S'}{\partial x}$ for the top 2 percentile intense and long heatwaves at 50N and 35N. The profiles only include heatwaves that survive till the nth day after heatwave start.

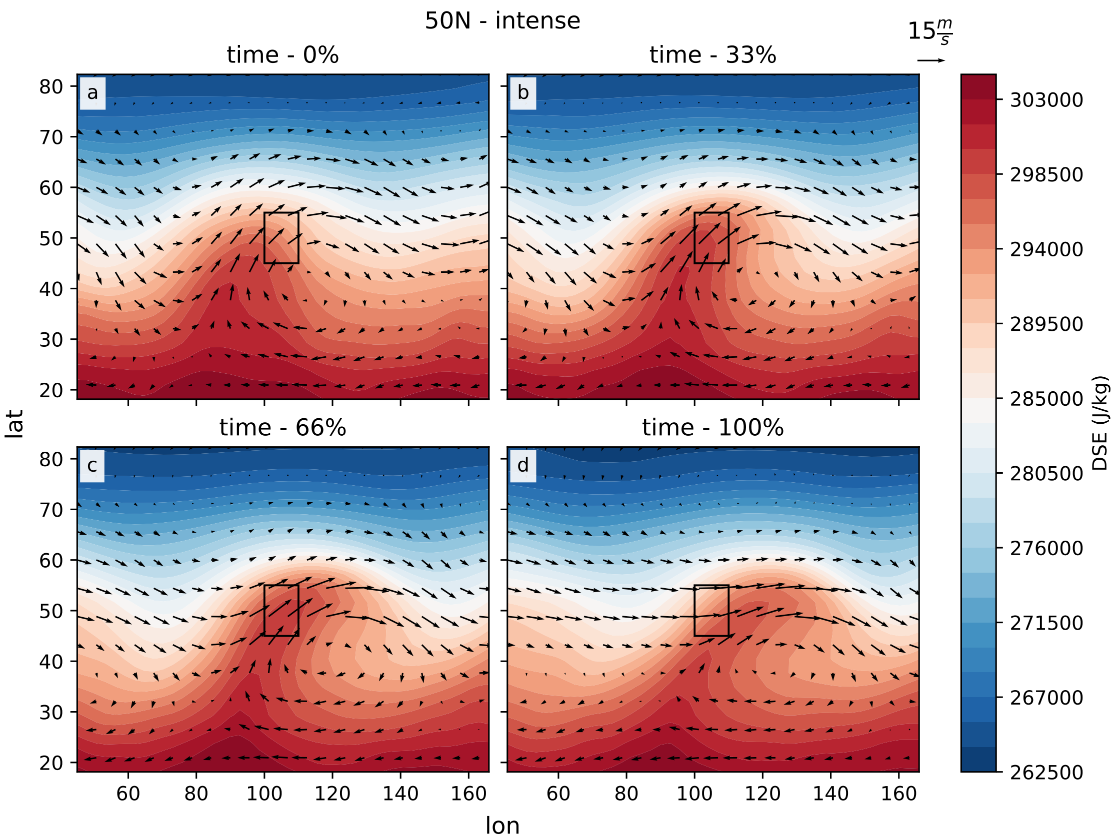

FIGURE S16: Intense heatwaves at 50N. The quivers show the total instantaneous winds averaged between 950hPa and 850hPa and the contours depict the total DSE between the same levels. The plots are drawn at equal time percentage intervals, with the duration of each heatwave in the composite normalised to be between 0% and 100%.

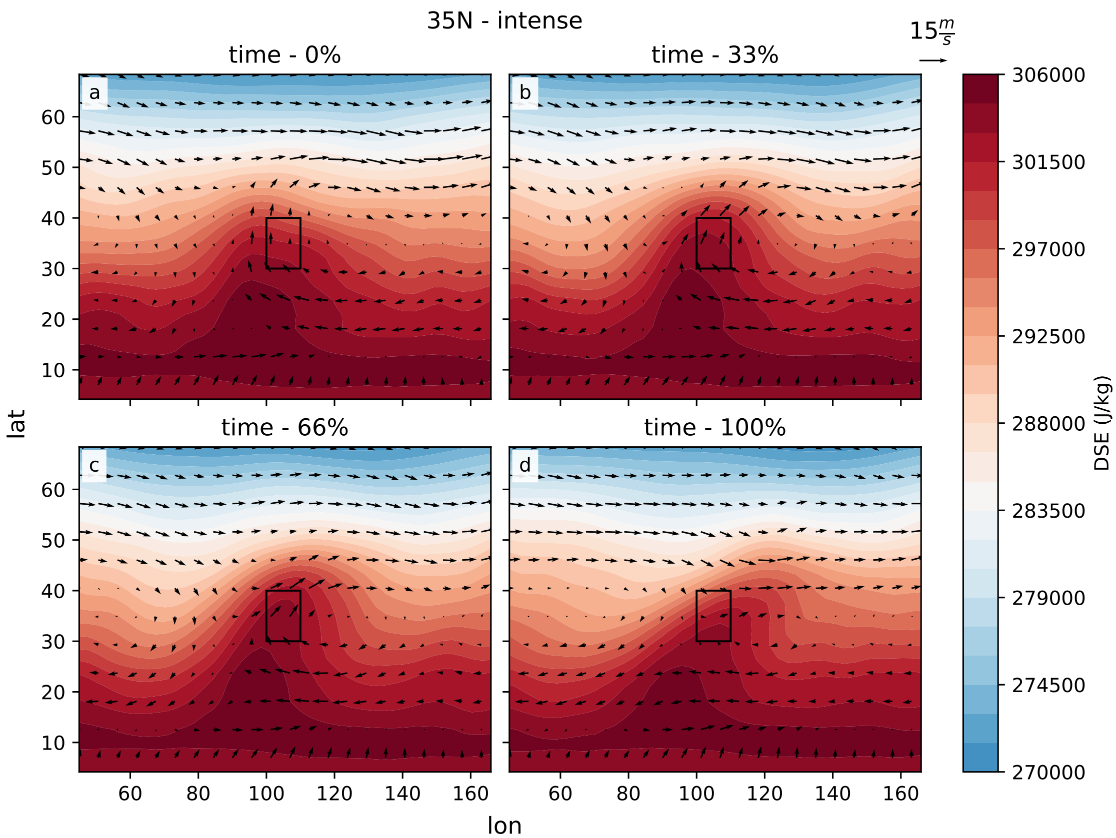

FIGURE S17: Intense heatwaves at 35N. The quivers show the total instantaneous winds averaged between 950hPa and 850hPa and the contours depict the total DSE between the same levels. The plots are drawn at equal time percentage intervals, with the duration of each heatwave in the composite normalised to be between 0% and 100%.

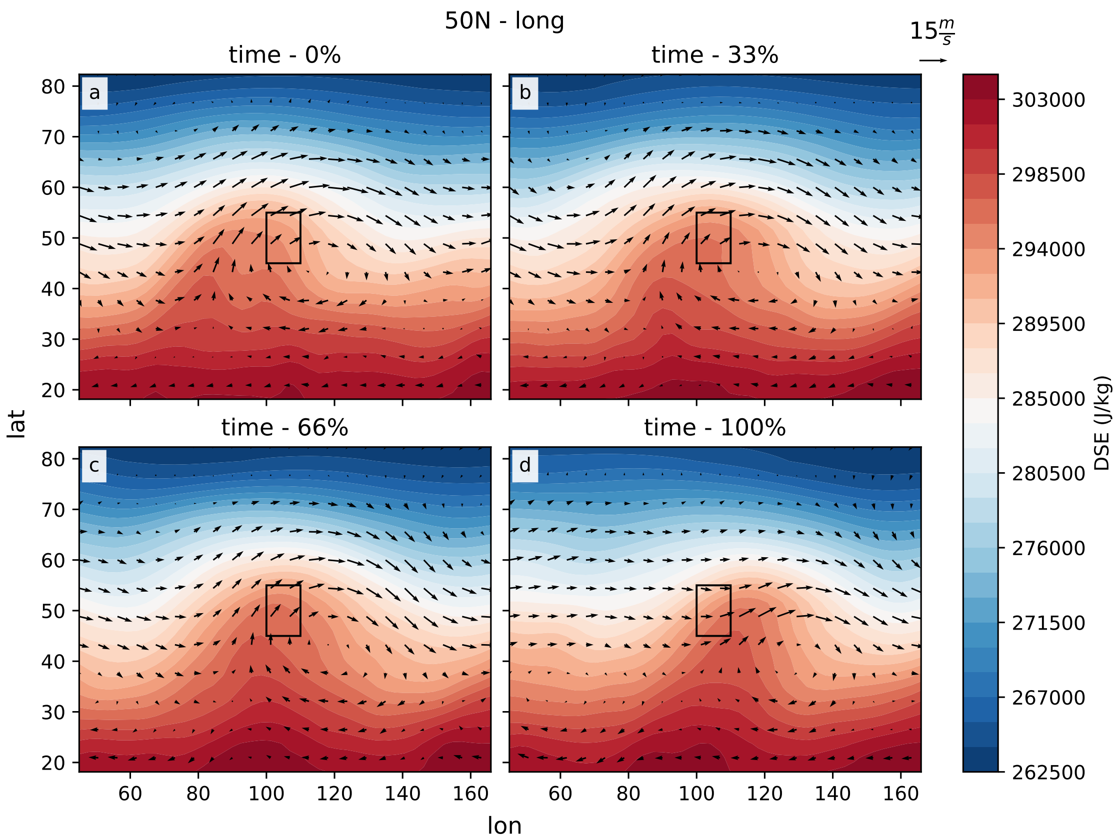

FIGURE S18: Long heatwaves at 50N. The quivers show the total instantaneous winds averaged between 950hPa and 850hPa and the contours depict the total DSE between the same levels. The plots are drawn at equal time percentage intervals, with the duration of each heatwave in the composite normalised to be between 0% and 100%.

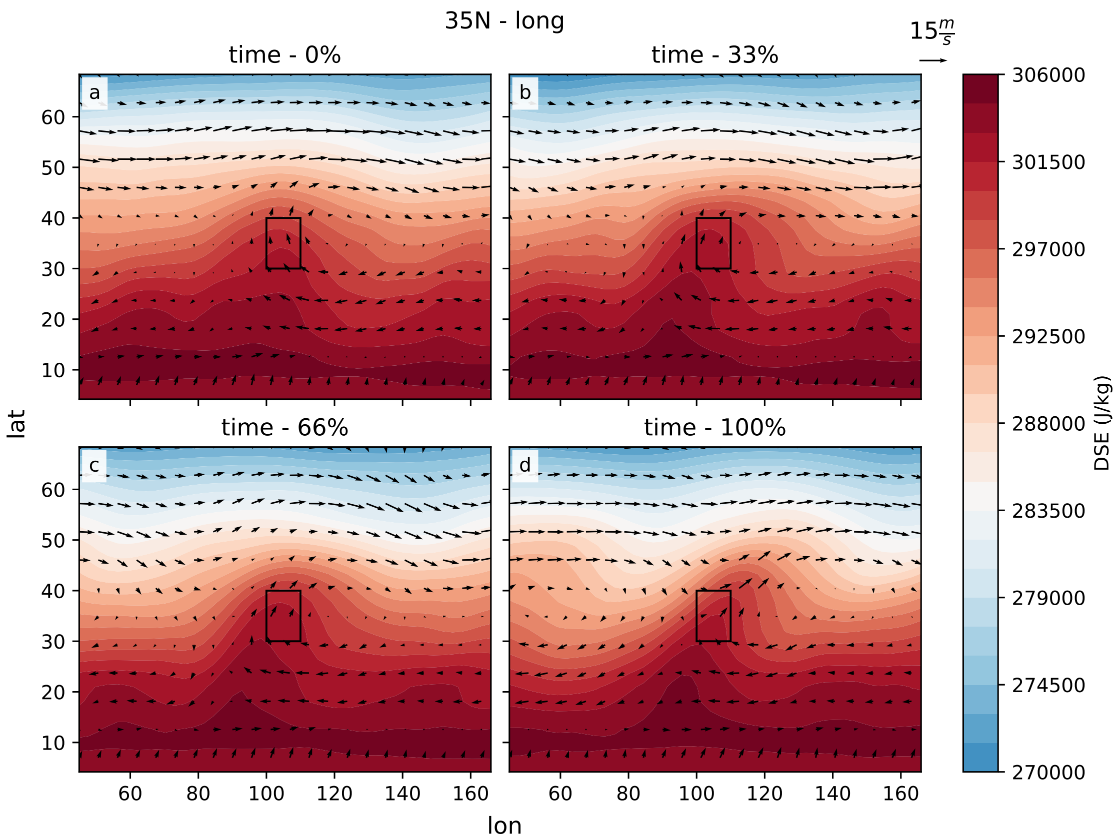

FIGURE S19: Long heatwaves at 35N. The quivers show the total instantaneous winds averaged between 950hPa and 850hPa and the contours depict the total DSE between the same levels. The plots are drawn at equal time percentage intervals, with the duration of each heatwave in the composite normalised to be between 0% and 100%.

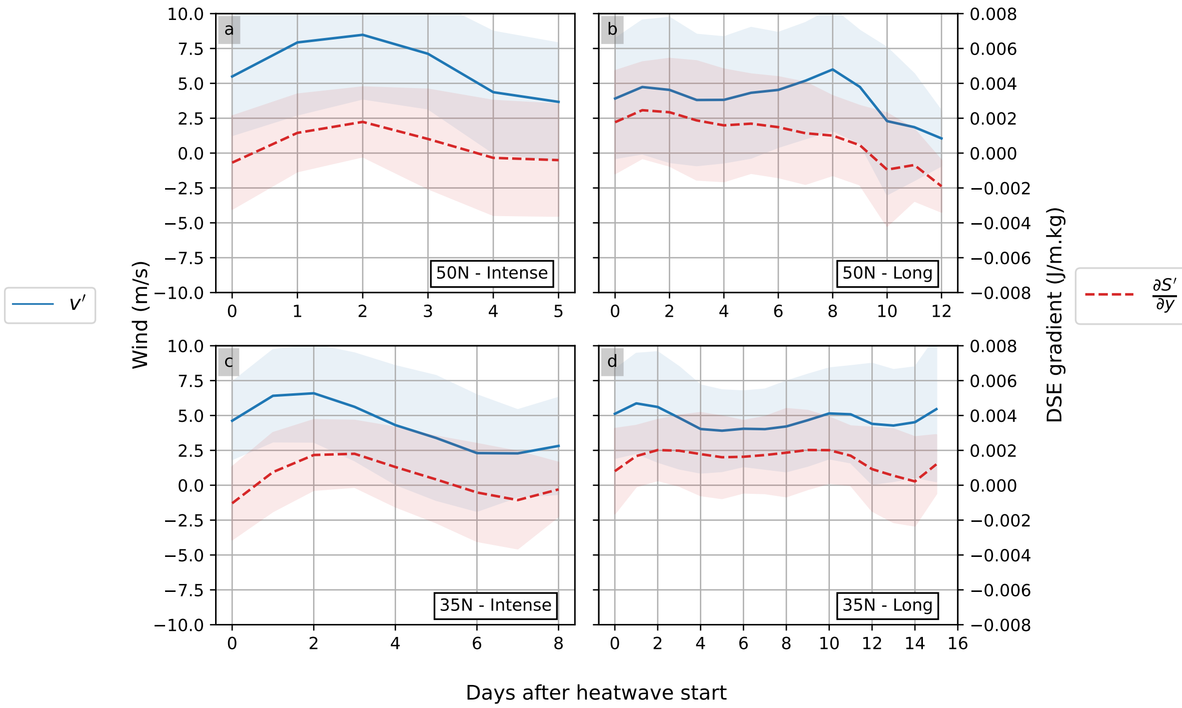

FIGURE S20: Patch-average profiles of v' and $\frac{\partial S'}{\partial y}$ for the top 2 percentile intense and long heatwaves at 50N and 35N. The profiles only include heatwaves that survive till the nth day after heatwave start. These quantities are calculated at the midpoints of consecutive heatwave days, resulting in a time grid staggered relative to heatwave days. The shading shows the standard deviation of these quantities across heatwaves.

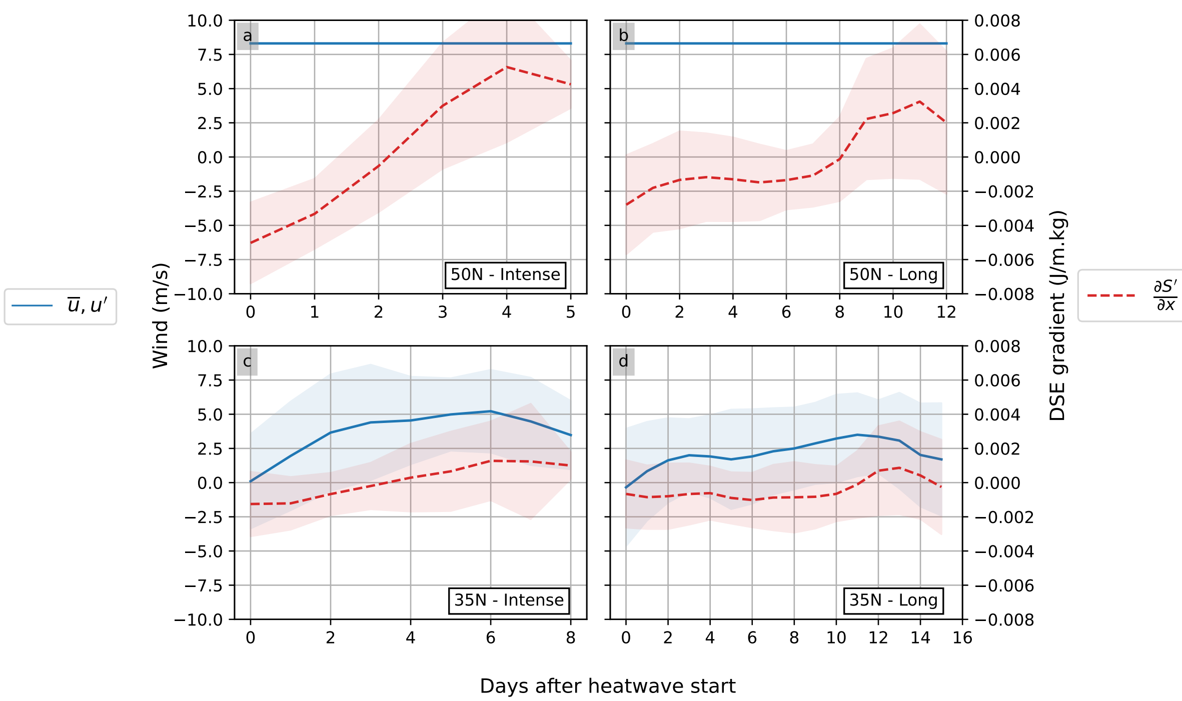

FIGURE S21: Patch-average profiles of $\overline{u}/u'$ ($\overline{u}$ at 50N, u' at 35N) and $\frac{\partial S'}{\partial x}$ for the top 2 percentile intense and long heatwaves at 50N and 35N. The profiles only include heatwaves that survive till the nth day after heatwave start. These quantities are calculated at the midpoints of consecutive heatwave days, resulting in a time grid staggered relative to heatwave days. The shading shows the standard deviation of these quantities across heatwaves.

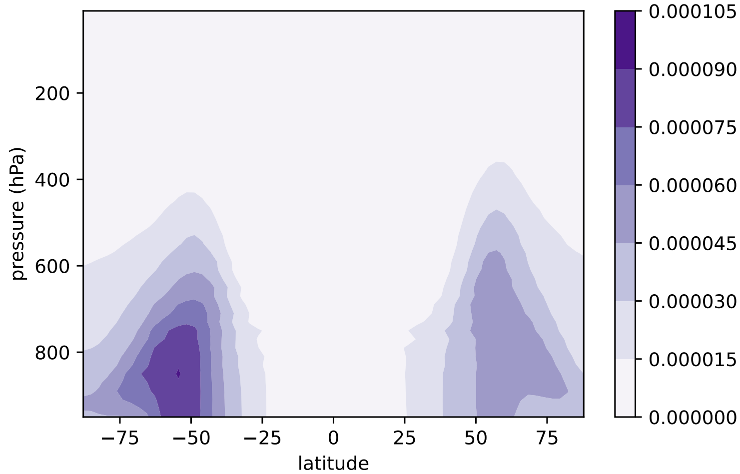

FIGURE S22: Zonal-mean variance of $\frac{\partial S'}{\partial x}$